Planetary and Space Science 109-110 (2015) 76–91

Contents lists available at ScienceDirect

Planetary and Space Science

journal homepage: www.elsevier.com/locate/pss

# A new analysis of Galileo dust data near Jupiter

R.H. Soja [a,b,*], D.P. Hamilton [c], N. Altobelli [a]

[a] European Space Astronomy Centre, European Space Agency, Madrid, Spain
[b] Institute of Space Systems, University of Stuttgart, Germany
[c] Department of Astronomy, University of Maryland, College Park, MD, USA

ARTICLE INFO

*Article history:*
Received 26 May 2014
Received in revised form
28 January 2015
Accepted 28 January 2015
Available online 27 February 2015

*Keywords:*
Jupiter dust
Dust dynamics

ABSTRACT

The Galileo Dust Detection System (DDS) detected a population of micron-sized grains in and amongst the orbits of Io, Europa, Ganymede and Callisto. Previous studies, using roughly 50% of the data now available, concluded that the dominant sources for the impacts were magnetospherically captured interplanetary particles largely on retrograde orbits (Colwell et al., 1998b; Thiessenhusen et al., 2000) and impact-generated ejecta from the Galilean satellites (Krüger et al., 1999b; Krivov et al., 2002a). Here we revisit the problem with the full data set and broaden our consideration to include four additional source populations: debris from the outer satellites, interplanetary and interstellar grains and particles accelerated outwards from Io and the jovian rings. We develop a model of detectable orbits at each Galileo position and we find that about 10% of the impact data require non-circular orbits with eccentricities greater than 0.1. In addition, ~3% of impacts require orbital solutions with eccentricities in excess of 0.7. Using the spatial distribution of particles, we are able to exclude, as dominant sources, all the additional source populations except for outer satellite particles. A study of DDS directional information demonstrates that none of the six standard sources fit the data well and thus a combination of sources is necessary. There are insufficient data to uniquely identify the relative strengths of the various contributions. However, we find an excess of large particles that is consistent with retrograde trajectories.



## 1. Introduction

Studies of dust populations within the Jovian system contribute to our understanding of dynamical behaviour, impact hazards, and the erosion and contamination of satellite and ring surfaces. The Galileo Dust Detection System (DDS) provided the best look at the dust environment outside of the main Jovian ring system, though a small amount of additional data was obtained from Pioneer 10 and 11 missions (Humes, 1980; Zeehandelaar and Hamilton, 2007). The Galileo mission was a NASA mission designed to study all aspects of the Jovian system. It completed 34 revolutions of Jupiter between 1996 and 2003, when the mission ended with the steering of the spacecraft into the Jovian atmosphere.

Galileo largely avoided the region within 9 Jupiter radii ($R_J$) of the planet in order to protect the spacecraft from the intense radiation environment. Beyond 9 $R_J$, Galileo detected a number of dust populations, including streams of very small and fast dust emanating from volcanism on Io (Grün et al., 1996a; Graps et al., 2000) (detected first by the Ulysses Dust Detector Grün et al., 1993), impact ejecta forming dust clouds around the Galilean satellites (Krüger et al., 1999b, 2003), and a number of impacts at the outskirts of the Jovian system consistent with ejecta from outer satellites (Krivov et al., 2002b). In the final part of the mission, the DDS also directly sampled particles in Jupiter's gossamer rings (Krüger et al., 2009). Furthermore, a distribution of micron-sized grains was found in the Galilean satellite region (~9–30 $R_J$) (Grün et al., 1996b, 1997).

Grün et al. (1998) and Colwell et al. (1998a) showed that a fraction of this latter population is inconsistent with prograde near-circular impacts. Further work suggested that these micron-sized grains consist of (1) a prograde population that could be mainly explained by impact ejecta from Galilean satellites (Krivov et al., 2002a); and (2) a retrograde population (Thiessenhusen et al., 2000) which may represent magnetospheric capture of interplanetary and interstellar dust particles focused by the strong Jovian magnetosphere (Colwell et al., 1998a,b).

These authors used DDS data from 1996–1999 (Thiessenhusen et al., 2000) and 1996–2001 (Krivov et al., 2002a). Because acquisition of data continued after 2001, these studies use only ~50%–90% of the complete data set and, accordingly, a reanalysis is warranted (Krüger et al., 2010). We also consider additional four dust sources that may contribute to this data, testing populations that are known to exist in the Jovian system, but which have not been unambiguously identified within the Galilean satellite region.

* Corresponding author at: Institute of Space Systems, University of Stuttgart, Germany. Tel.: +49 711 685 65860.
*E-mail address:* soja@irs.uni-stuttgart.de (R.H. Soja).

http://dx.doi.org/10.1016/j.pss.2015.01.020
0032-0633/

These additional sources are (3) material from outer Jovian satellites (Krivov et al., 2002b), (4) particles escaping from Jupiter's gossamer rings (Hamilton and Burns, 1993; Hamilton and Krüger, 2008), and (5) focused interplanetary or (6) interstellar particles traversing near-Jupiter space. All additional sources predict primarily radial orbits which may be required by the data. Here we investigate whether the observed distributions of particles are consistent with the expected distributions for each of the six sources identified above. Due to the lack of constraints on the direction of observed particles, it is not expected that we will be able to uniquely identify the source for individual particles. Rather, we aim to place statistical constraints on how various populations contribute to the dataset as a whole.

## 2. Galileo DDS

The Galileo DDS is an impact ionisation detector that can detect dust particles when they vaporise on contact with the detector target and produce a plasma cloud. The plasma particles are detected by up to three charge detectors (ion charge, electron charge, and channeltron). While the electron and ion charges are used to estimate the particle speed and mass, the channeltron detection only assists with impact identification (Grün et al., 1995). Dust accelerator tests for different projectile materials were used to calibrate the impact speed as functions of the ion and electron risetimes $t_I$ and $t_E$, which can be used to produce ion and electron speed measurements $v_{t_I}$ and $v_{t_E}$ (Göller and Grün, 1989). The impact speed is taken as a geometric mean of these measurements: $v=\sqrt{v_{t_I} v_{t_E}}$. Calibration curves are used also to relate the impact speed $v$ to the ratio of charge to mass $Q_I/m_{Q_I}$ and $Q_E/m_{Q_E}$. The measured mass is then the geometric mean: $m=\sqrt{m_{Q_I} m_{Q_E}}$. This calibration can be approximated by

$$Q_I \propto m^{\alpha} v^{\beta} \tag{1}$$

where $\alpha \approx 1$ and $1.5 \leq \beta \leq 5.5$ for the calibrated speed range $2 \leq v \leq 70$ km s$^{-1}$ (an average of $\beta \sim 3.5$ is often assumed) (Grün et al., 1995). In practice, speed and mass measurements have large uncertainties, but the ion charge amplitude $Q_I$ is more robust. Individual velocity measurements are typically accurate to a factor of 2, and mass values to a factor of 10. Impact velocity vectors are constrained by the 140° opening angle of the detector (although wall impacts can increase this angle, see below). Further instrument details are given in Grun et al. (1992, 1995).

Galileo DDS impacts are described by two characteristic classes. The 'charge class number' CLN describes the number of independent charge signals registered for that event. Charge classes 0 and 1 are noise within the inner Jovian system (but real impacts outside ~50 $R_J$); while charge classes 2 and 3 register real dust impacts everywhere. We use a denoised data set including all $CLN \geq 2$ impacts that are expected to represent dust impacts (Krüger et al., 1999a, 2005. Previous work has demonstrated that the sensitive area (and thus the effective opening angle) of the detector for $CLN=3$ impacts may be smaller than for $CLN=2$ impacts (Krüger et al., 1999a). However, this is only demonstrated fully for tiny $AR=1$ impacts (corresponding to Jovian dust streams) and thus we utilise all $CLN \geq 2$ data and the full sensor field of view. In Section 5 we also use the full data set including all DDS 'events' (all CLN classes), with the understanding that inwards of ~30$R_J$ those with $CLN < 2$ are noise events.

Each impact is also classified by its ion charge signal $Q_I$ into six 'amplitude ranges' (AR), each corresponding to approximately one order of magnitude in impact charge. AR=1 consists mostly of small Jovian stream particles (Grün et al., 1996a), while larger particles are found in $AR=2$ to $AR=6$. Particles detected in a higher impact charge class must have either a higher mass or a higher speed (or both) than those particles in a lower class (see Eq. (1)).

Three instrumental effects that can affect interpretation of the results are noise; electronics ageing and incomplete data transmission. The first is understood, and affects the smallest impacts most strongly. It is largely a result of the radiation environment of the Jovian system. As described above, class 1 and 0 are assumed to be noise in the jovian environment, although they are real impacts outside ~50 $R_J$. Krüger et al. (1999a) describe how noise events can be reliably removed from class 2 impacts. Class 3 impacts are usually noise free.

Electronics ageing as a result of the Jovian radiation environment increases with time and affects the classification of individual particles. As an illustration, no $AR=5$ or $AR=6$ impacts are observed in 2000–2003 as a result of this degradation (although very few were observed before these dates). This effect is difficult to quantify, but will be considered qualitatively in our analysis.

Full data from all impact events was not transmitted to Earth as a result of Galileo's low transmission capabilities. However, information was retained on the full number of impacts in order to assess the completeness of the data. This varies strongly depending on the time period and $AR$ class: for $CLN=3$ particles, from 1996–1999 $AR>1$ is almost fully transmitted; from 2000 to 2003, transmission rates for $AR=2,3$ and 4 are ~84%, ~70% and ~47% respectively. Over all years the transmission rates for $AR=2,3$ and 4 are ~94%, ~91% and ~65% for $CLN=3$, and ~23%, ~46% and ~23% for $CLN=2$.

In addition, it is possible for impacts on the side wall to register as events. This can increase the apparent field of view of the instrument, and decrease the number density. This has been studied for interstellar particles (Altobelli et al., 2004) and Gossamer ring particles (Krüger et al., 2009). For Galileo, it was found that perhaps 27% of impacts could be wall impacts (Willis et al., 2005). This affect our ability to assign particles to different populations, because the incoming particle direction uncertainty is increased.

### 2.1. Dust detector geometry

The Galileo spacecraft has a spin axis that, in general, points in the anti-Earth direction. The DDS is mounted at an angle of 60° from the spin axis (Krüger et al., 1999a). The rotation angle $ROT$ describes the position of the detector with respect to the spin axis, and is approximately 0 in the direction of ecliptic north. The direction of increasing rotation angle is opposite to the spin direction of Galileo (Grün et al., 1995). This ROT angle is described further in Thiessenhusen et al. (2000); Krivov et al. (2002b), and in particular by their Fig. 2 and 1 respectively. We refer the reader there for a comprehensive view.

The sensitive area of the detector has a maximum of 0.1 m$^2$ and is a decreasing function of angle from the sensor axis, such that 50% of all particles from a theoretical isotropic distribution impact within 32° of the sensor axis, with an average angle of 36° (Grün et al., 1992). The sensitive area is non-zero for particles that have angles of impact with the sensor axis of less than 70°. However, the sensitive area is increased by the presence of wall impacts, with impacts having non-zero sensitive area up to an impact angle of 90° (Altobelli et al., 2004). We use a sensitive area inclusive of this effect, as given in Fig. 6 of (Altobelli et al., 2004).

The relative velocity of Galileo also affects the probability of detecting a given orbit. Thus, we use an 'effective sensitive area' that accounts for the relative motion of Galileo. As defined in Altobelli et al. (2005), this provides the detector area required to register the same impact rate as in the jovicentric inertial frame, and is given by

$$A_{eff}(V_{imp}, \phi, t) = \frac{|V_{imp}|}{|V_d|} A(\phi, t) \tag{2}$$

where $V_{imp}$ and $V_d$ are the impact velocity and jovicentric dust velocity respectively, and $A(\phi, t)$ is the sensitive area of the detector (a function of impact angle $\phi$ and time $t$).

### 2.2. Data set

We extract $AR \geq 2$ impacts from a denoised data set including all $CLN \geq 2$ impacts that are expected to represent real dust impacts (Krüger et al., 1999a, 2005). We remove those within the Hill spheres of the Galilean satellites and registered during passes of the spacecraft through the Gossamer ring plane to avoid contamination from these known sources (Krüger et al., 2003, 2009). Jovian dust stream particles affect primarily the $AR=1$ data and so are largely absent from our data set. Except in Section 5, which examines the radial distribution of observed impacts, we restrict the dataset to impacts within 50 $R_J$ of Jupiter (to approximate the Galilean satellite region). The resulting data set includes 273 $AR=2$ impacts, 89 $AR=3$ impacts, 60 $AR=4$ impacts, 17 $AR=5$ impacts and 6 $AR=6$ impacts. In Section 5 we use the entire dataset within 2400 $R_J$, which has 367 $AR=2$ impacts and 208 $AR \geq 3$ impacts, in the data set with $CLN \geq 2$.

## 3. Modelling detectable orbits using DDS directional data

We are interested in whether certain types of orbit (defined by combinations of orbital elements) are visible to the Galileo DDS at the location of each impact. This defines the set of orbits that can describe the observed impact. The DDS pointing direction and opening angle are the only constraints on the incoming particle direction. Since this opening angle is large (140° - and expanded to ~180° by the presence of wall impacts), it is not possible to define a narrow range of orbital elements for each observed dust grain; we can only draw general conclusions on the statistical properties of the orbits required to explain a large set of particles.

We define our test populations in terms of limits on the orbital elements: the semimajor axis $a$, the eccentricity $e$, and the inclination $i$. We test each DDS impact individually. Steps to produce this model are as follows. For each population, and at each position of Galileo at the time of a measured DDS dust impact, we:

- Randomly choose a set of 100,000 orbits from within a population of orbital element limits, each representing a simulated impacting particle.
- Calculate the true anomaly, and the radial $v_r$, polar $v_\theta$, and azimuthal $v_\phi$ velocity components for each model orbit. For a given $(a, e, i)$ there are four possible ways for a particle to meet Galileo corresponding to dust moving inwards ($v_r < 0$) or outward ($v_r > 0$) and upward ($v_\theta < 0$) or downward ($v_\theta < 0$).
- We remove orbits that cannot intersect at the current Galileo location. For the remaining orbits, we calculate the jovicentric, Cartesian velocity coordinates $v_x$, $v_y$ and $v_z$, and the impact velocities relative to Galileo. At this stage, we have the full set of orbits that can strike the Galileo spacecraft, as well as the relative velocity vector for each possible impact.
- Calculate the impact angle between the Galileo pointing direction, and the relative velocity vector, and use this to calculate the sensitive area for each of the four orbital solutions using Eq. (2). Particles that fall within the opening angle of the detector (including correction for wall impacts) are defined to have non-zero sensitive area.

This process requires the position and velocity of the Galileo spacecraft, and the pointing direction of the Galileo DDS, in a fixed jovicentric frame. We use the jovicentric ecliptic J2000 frame: Jupiter's low inclination ( ~ 1.31°) ensures that this is very close to Jupiter's equatorial frame.

## 4. Analysis

Our aim is to constrain the orbital parameters of impacting dust grains observed by the DDS. The most important orbital elements in this regard are the eccentricity and inclination. The eccentricity provides information on how close to circular these orbits are, while the inclination tells us if the orbits are planar or inclined, and prograde or retrograde. We divide the DDS data into $AR=2$ and $AR \geq 3$ subsets because previous studies have suggested that these particles each come from dynamically different populations (Thiessenhusen et al., 2000).

We begin by asking whether the impacts can be described by circular, planar, prograde orbits. Grün et al. (1998) and Colwell et al. (1998a) find, using directional arguments (see Section 6), that the data must also contain some particles on eccentric and/or inclined orbits. We use the approach outlined in Section 3 to extend this argument to orbits with arbitrary eccentricity and inclination. We randomly draw orbits from a uniform distribution with semi major axes between 4 and 200 AU, eccentricities from 0 to 1, and inclinations from 0 to 180°. For the conditions of each DDS impact, we determine the subset of these calculated dust orbits that successfully meet Galileo with an impact direction that falls within the 140° field of view. We use this to determine the fraction of these impacts that can be explained by an orbital eccentricity less than some threshold. Fig. 1 indicates that $AR=2$ and $AR=3-6$ are dynamically different, and shows that retrograde orbits are, in general, less consistent with the data than prograde orbits and that both high eccentricities and high inclinations are favoured.

We find that ~90% of $AR=2$ and ~95% of $AR \geq 3$ can be explained by prograde orbits with eccentricities $< 0.1$. For $AR=2$ impacts, eccentricities up to ~0.7 are required to explain 97%. This is evidence that (1) we require a source that can produce particles that are not on circular, prograde orbits, and (2) that there must be a source that can produce impacts that are very highly eccentric, with eccentricity $e > 0.7$. Restricting the possible orbits to low inclination solutions simply exacerbates the problem such that only ~76% of $AR=2$ and ~82% of $AR \geq 3$ can be explained by prograde orbits with eccentricities $< 0.1$ and inclinations $< 20°$.

### 4.1. Six dusty populations

We want to determine what sources can explain the observed small $AR=2$ and large $AR \geq 3$ impacts. To improve on Fig. 1, we now consider the six populations discussed in Section 1. Orbital parameters used for each of these sources (except for interstellar dust, which is modelled separately) are given in Table 1. The population of dust raised by impacts into the Galilean satellites can attain moderate eccentricities and inclinations by repeated gravitational scatterings (Krivov et al., 2002a; Zeehandelaar and Hamilton, 2007) and we choose our orbital element ranges in Table 1 accordingly. Dust lofted from the outer satellites must be driven to high eccentricity by radiation pressure to reach our region of interest inside $50R_J$, while the orbital elements for the Gossamer ring source are appropriate for dust escaping along hyperbolic orbits from pericentre at $3R_J$. The range of orbital elements for interplanetary capture are taken to match results from Colwell et al. (1998b). Finally for interplanetary trajectories we choose hyperbolas orbits with moderate speeds of 2–10 km/s at infinity that move through our region of interest. These populations are approximate, but are sufficient for our purposes given the uncertainties inherent in the Galileo dust data. We now discuss these six sources in more detail.

#### 4.1.1. Galilean satellites (GS)

Impact-generated ejecta near the Galilean satellites have been observed (Krüger et al., 1999b, 2000, 2003), and described by the models of Krivov et al. (2003); Sremčević et al. (2003, 2005). Additionally, Krivov et al. (2002a) show that $AR=2$ impacts in the Galilean satellite region (but far from the satellites) can be explained by escaped ejecta from the Galilean satellites. This source (GS in Table 1) produces low-eccentricity ($<0.3$) prograde orbits with low inclinations ($<30^\circ$) (as determined by Zeehandelaar and Hamilton (2007)). Semimajor axis limits are chosen to match the approximate locations of the Galilean Satellites.

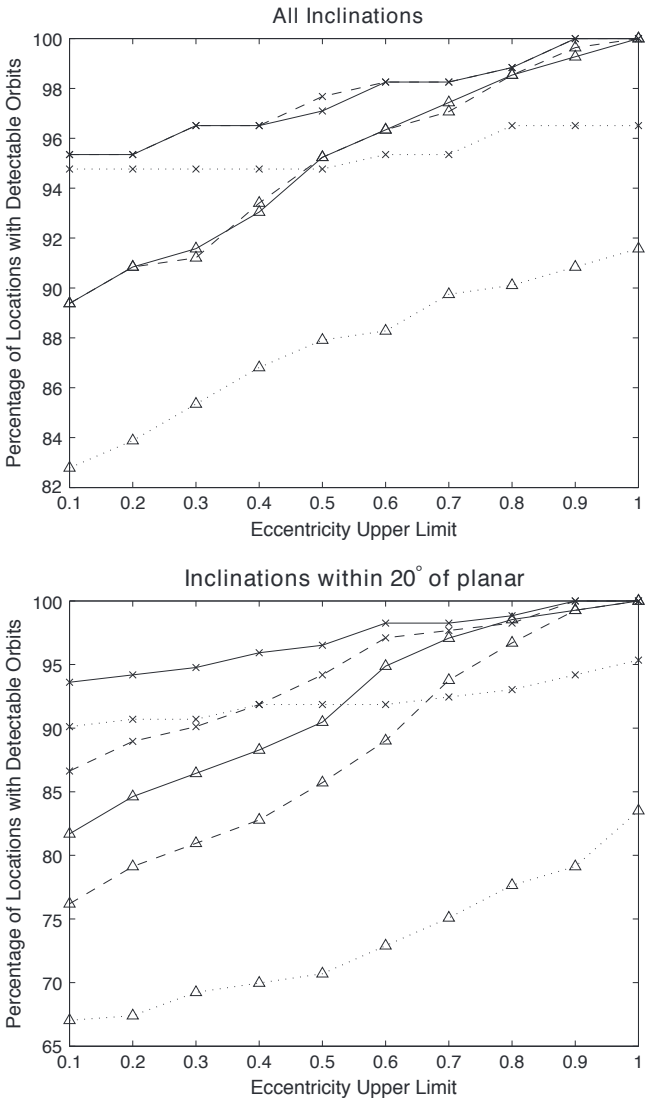


**Fig. 1.** Number of impacts that can be explained by prograde ($i<90^\circ$) and retrograde orbits ($i>90^\circ$) with different maximum eccentricities. Triangles represent the results for $AR=2$ data, and crosses the results for $AR\geq 3$ data. Dotted, dashed and solid lines represent respectively results using retrograde orbits only, prograde orbits only, and all orbit types. The upper figure is the results using all inclinations, while the lower figure uses only orbits with inclinations within 20° of planar.

#### 4.1.2. Outer satellites (OS)

The presence of impact-generated ejecta induced by interplanetary impactors at both the Galilean satellites and the inner satellites (thus forming the gossamer rings Burns et al., 1999) encourages the opinion that such a process may also occur at the outer satellites; this is our OS source in Table 1. Indeed, Krivov et al. (2002b) find that Galileo DDS measurements in the outer Jovian system can be explained by ejecta from these outer satellites. Small outer satellite particles that reach the Galilean satellite region usually have highly eccentric orbits. Both prograde and retrograde dust should be present. At Saturn the retrograde satellite Phoebe is observed to create a ring of retrograde particles in this manner (Verbiscer et al., 2009). Bottke et al. (2010), who studied the evolution of collisionally generated particles in an early, highly dense Jovian outer satellite region, demonstrate how this dust could have migrated inwards under radiation forces and coated the inner satellites, in a manner consistent with observations. The selected semi-major axis limits in Table 1 reflect the locations of these satellites. Eccentricities are chosen such that these particles can reach the Galilean satellite region, and inclinations reflect typical satellite inclinations.

#### 4.1.3. Ring source (RS)

Submicron particles from Io and the Jovian gossamer rings are accelerated into interplanetary space by strong electromagnetic forces (Horányi et al., 1993; Hamilton and Burns, 1993). Grain charging effects in Jupiter's shadow raise the maximum size of escaping grains from a few tenths of a micron to a few microns (Hamilton and Krüger, 2008; Jontof-Hutter and Hamilton, 2012a,b). Unlike the tiny 10 nm grains that comprise dust streams these larger, but rarer, particles might be detected in the DDS $AR\geq 2$ amplitude ranges; this is our ring source (RS) in Table 1. We choose their eccentricities such that their perijoves are in Thebe's gossamer ring at 3.0 $R_J$. Inclinations up to 20–30° are expected as a result of a vertical shadow resonance (Hamilton and Krüger, 2008). Small but negative semimajor axes indicate strongly hyperbolic orbits. We ensure that these orbits only head outwards by restricting the radial velocity to be positive in our analysis.

#### 4.1.4. Interplanetary capture (IC)

Magnetospheric effects can focus or defocus the orbits of small interplanetary grains near Jupiter Hill and Mendis, 1979, 1980;

**Table 1**
Orbital parameters used to constrain five of the populations (three with prograde and retrograde components) tested here. The Interstellar (IS) dust population is separately constrained by modelling the expected direction and velocity of the incoming IS dust flow. Landgraf (2000), Altobelli et al. (2005) and Sterken et al. (2012).

| Population | | Semi-major axis ($R_J$) | Eccentricity | Inclination (°) |
|---|---|---|---|---|
| Galilean satellites (prograde) | GS | 5–30 | 0–0.3 | 0–30 |
| Outer satellites (prograde) | OS | 100–200 | 0.90–0.99 | 0–30 |
| Outer satellites (retrograde) | | 100–400 | 0.90–0.99 | 150–180 |
| Ring source | RS | −10 to −0.5 | $e=1+3.0R_J/a$ | 0–30 |
| Interplanetary capture (prograde) | IC | 5–25 | 0–0.8 | 0–20 |
| Interplanetary capture (retrograde) | | 5–25 | 0–0.8 | 140–180 |
| Interplanetary flyby (prograde) | IF | −500 to −20 | 1.01–1.1 | 0–90 |
| Interplanetary flyby (retrograde) | | −500 to −20 | 1.01–1.1 | 90–180 |

Colwell et al., 1998b. A ring of magnetospherically captured interplanetary and interstellar particles in the Galilean satellite region was first proposed by Horanyi (1994), and further developed by Colwell et al. (1998a) and Colwell et al. (1998b). This source is particularly interesting as it would produce a majority of retrograde particles on near-planar, low-moderately eccentric orbits. Thiessenhusen et al. (2000) found that $AR \geq 3$ particles could be explained by retrograde particles from this source.

The model of Colwell et al. (1998b) demonstrates that this capture mechanism should produce a tenuous ring (with a maximum optical depth of $\sim 10^{-9}$) consisting mostly of 0.6–1.4 μm grains, confined within $\sim 20$ $R_J$, with a broad eccentricity distribution with eccentricities up to $\sim 0.8$, and with both prograde and retrograde particles in two inclination populations: 0–20° and 140°–180°. They expect captured particles to have short lifetimes: representative values are $\sim 100$ years for prograde particles and $\sim 25$ years for retrograde particles.

#### 4.1.5. *Interplanetary flyby (IF))*

Jupiter's gravitational focusing can significantly enhance the number of interplanetary particles flying through the Galilean satellite region. The trajectories of interplanetary grains are modelled as hyperbolas. We limit the velocity at infinity to 2–30 km $s^{-1}$ (30 km $s^{-1}$ is the maximum velocity relative to Jupiter expected for comet-like orbits) and the minimum radial distance to $r_{min} < 50$ $R_J$ (within the region of the Jovian system we are interested in): this provides semi-major axis and eccentricity ranges of $a = -500$ to $-20$ $R_J$ and $e < 1.1$.

#### 4.1.6. *Interstellar source (IS)*

The direction and speed of interstellar particles flying through the Solar System can be modelled (Landgraf, 2000; Altobelli et al., 2005; Sterken et al., 2012). We use models of the speed and direction of interstellar dust through the Solar System for the time of each Galileo DDS impact, assuming $\beta = 0.9$ (where $\beta$ is the ratio of radiation force to gravitational force).

We model the non-IS sources using the orbital element combinations given in Table 1. We determine what percentage of $AR = 2$ and $AR \geq 3$ impacts can be explained by each source (Fig. 2). Can a single source explain 90% of the impacts? It is clear that Galilean satellite particles on prograde, near-circular orbits cannot explain all observed impacts, in particular for the $AR = 2$ population. Highly eccentric sources, such as outer satellite impacts, are able to explain all impacts, as geometrically their high-speed orbits can more easily enter the detector field of view. Because of geometrical constraints, Jovian ring particles are less successful, but still able to explain most impacts. An interplanetary source with both prograde and retrograde particles can also explain nearly all of the impacts.

Interstellar dust grains are the least successful at explaining the impacts: this is expected as the geometry of Galileo is poor for detection of interstellar grains for two reasons. First, the pointing direction of the spacecraft is such that the interstellar dust stream was only visible from 1995 to 2000. In addition, the heliocentric velocity of the spacecraft was in approximately the same direction as the interstellar dust velocity during the period 1996–2001, resulting in a minimum jovicentric velocity of 13 km $s^{-1}$ and correspondingly fewer and weaker impacts.

However, it is also apparent from Fig. 2 that many impacts have more than one possible source, as the 180° effective opening angle restricts our ability to strongly constrain the orbital properties of impactors. We therefore aim to understand the most likely sources contributing to the $AR = 2$ and $AR \geq 3$ data sets. We will take two main approaches to this analysis, investigating first the radial distribution of impacts, and then revisiting the more complicated directional information.

## 5. Radial distribution

We begin by comparing the observed radial distribution of DDS impacts to theoretical distributions that we will construct from the populations summarised in Table 1. We combine the $AR = 2$ and $AR \geq 3$ data to improve our statistics since, as can be seen in Fig. 3, the two distribution are similar. This radial distribution is determined by (i) the distribution of source orbits, by (ii) dynamical effects that can alter the orbits after their production or entrance into the Jovian system (and may also lead to destruction or loss of particles), by (iii) the pointing of the DDS, and by (iv) the time Galileo spends at each distance from Jupiter.

Since we find that the radial distribution is similar for different $AR$ classes, we again consider whether one population can describe all impacts. The number of impacts as a function of particle mass is

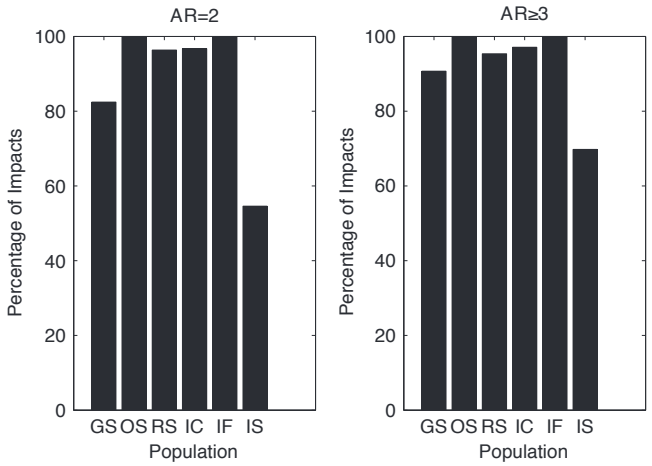


**Fig. 2.** Percentage of $AR = 2$ and $AR \geq 3$ data sets that can be dynamically explained by each of six different orbital populations (abbreviations and parameters given in Table 1).

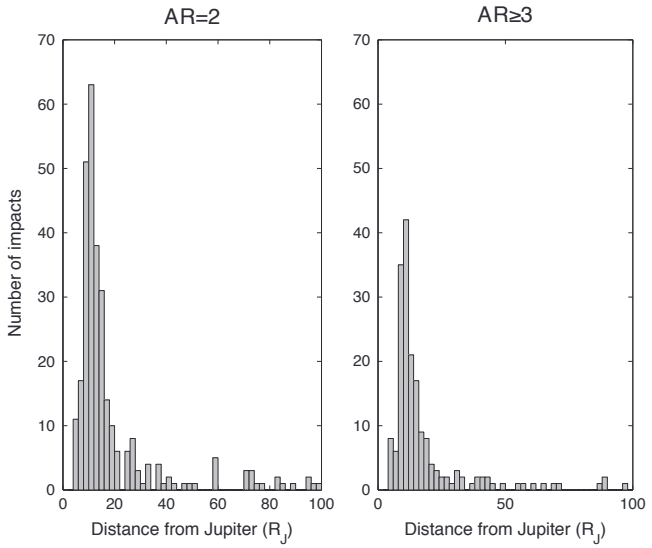


**Fig. 3.** Radial distribution of observed DDS impacts present in the Jovian system, for the $AR = 2$ and $AR \geq 3$ data sets. Note that this does not represent an accurate radial distribution of dust grains in the Jovian system, as the number of impacts is affected by Galileo sampling and geometry. The data used the denoised data set, with impacts that occur during passes of the spacecraft through the Hill Sphere of Galilean satellites or the Gossamer ring plane removed, as described in Section 2.2.

assumed to be governed by a power law distribution, with a mass distribution index $\gamma$ in the range 0.4–1.0 (Krivov and Jurewicz, 1999; Koschny and Grün, 2001), although a value of 0.8 is often used (Krivov et al., 2002a). The masses of $AR=3$ particles are an order of magnitude higher than the masses of $AR=2$ particles, and so on (assuming the same speeds for both sets of particles, which is reasonable in the case of the same source). Using a logarithmic mass distribution with mass distribution indices $\gamma = 0.8$ (a 'typical' value), $\gamma = 0.5$ (an intermediate value) and $\gamma = 0.4$ (the minimum value), we calculate the number of particles expected in each *AR* class, starting from the number of impacts in $AR=2$: that is, if all particles are from the same source, how many do we expect in each *AR* class? We compare these with the observed numbers of particles in each bin (Table 2). We can see that the observed number of particles for $AR=3$ falls within the range of calculated theoretical values: thus, it is possible that $AR=2$ and $AR=3$ particles have the same source, especially if gamma ~0.5. There is, however, a strong excess in the number of $AR=4$ particles, which may indicate the presence of a second distinct source of particles. The numbers of particles in $AR=5$ and $AR=6$ are on the limit of the expected numbers of particles; some of these particles may come from a second source also. We note that number statistics are low in these highest *AR* classes.

Instrument degradation is likely to push later particles to lower *AR* bins. This could weaken this conclusion, although it is difficult to quantify the effect. We test an unrealistic 'worst-case scenario' in which all particles are shifted to the preceeding *AR* class, and find that in this case the difference between $AR=3$ and $AR=4$ would be removed (although the numbers of $AR=5$ are then larger than expected). However, we find that transmission rates (calculated combining $CLN=2$ and $CLN=3$) are much higher for $AR=3$ (~79%) than for $AR=4$ (~48%) (Krüger et al., 2001, 2006, 2010). This strengthens the difference between $AR=3$ and $AR=4$, such that we observe more $AR=4$ than $AR=3$ (see Table 3). Although the calculated numbers in Table 3 show that AR=4 could match the number of satellite particles with $\gamma = -0.4$, the low number of AR=3 impacts means that this is not likely to indicate that $AR=4$ particles originate from the Galilean satellites. On balance, we consider it likely that the excess of $AR=4$ impacts is real.

A possible 'single' source could be Galilean satellite ejecta, which Krivov et al. (2002a) found to be the dominant source for $AR=2$ impacts. Krivov et al. (2002a) also modelled this theoretical radial distribution of these particles and concluded that this scenario is consistent with the observed radial distribution for $AR=2$ impacts. The presence of Galilean satellite ejecta in the higher $AR=3$ class may be consistent with the work of Zeehandelaar and Hamilton (2007), who modelled the distribution of large Pioneer dust impacts by Galilean satellite ejecta. Thus, this source may potentially explain most impacts, although the excess number of $AR=4$ impacts is still problematic.

**Table 2**
Do the numbers of expected impacts agree with the theoretical numbers if all impacts are from the same source? We give the total number of impacts in each *AR* class, and the number expected in that *AR* class for each of three mass distribution indices ($\gamma = 0.4, 0.5, 0.8$). All calculated results have been scaled to the observed 273 AR=2 impacts. The data used the denoised data set, with impacts that occur during passes of the spacecraft through the Hill Sphere of Galilean satellites or the Gossamer ring plane removed, as described in Section 2.2.

| AR class | Observed number | Calculated number ($\gamma=0.4$) | Calculated number ($\gamma=0.5$) | Calculated number ($\gamma=0.8$) |
|---|---|---|---|---|
| 3 | 89 | 109 | 87 | 43 |
| 4 | 60 | 44 | 28 | 7 |
| 5 | 17 | 17 | 9 | 1 |
| 6 | 6 | 7 | 3 | 0 |

**Table 3**
Do the numbers of expected impacts agree with the theoretical numbers if all impacts are from the same source? Here we repeat Table 2, but use the observed numbers of particles corrected for incomplete transmission. Low number statistics mean that the transmission rates for $AR=5$ and $AR=6$ are unreliable.

| AR class | Corrected number | Calculated number ($\gamma=0.4$) | Calculated number ($\gamma=0.5$) | Calculated number ($\gamma=0.8$) |
|---|---|---|---|---|
| 3 | 114 | 327 | 260 | 130 |
| 4 | 125 | 130 | 82 | 21 |

### 5.1. Exogenic sources

Interplanetary and interstellar particles have been measured in interplanetary space near Jupiter by Ulysses and Galileo. Both populations should transit the Jovian system on hyperbolic orbits. At great distances these grains have a uniform distribution, but near Jupiter they will be affected by gravitational focusing, to a degree dependent on their velocity at infinity. It therefore may be possible for these sources to have a peaked radial distribution at Jupiter such as is seen in Fig. 3.

To accurately compare measured and theoretical radial distributions, they must both correspond to the same range of particle masses. Since *AR* classes are based on charge measurements, our current selection of impacts ($AR \geq 2$) will be biased because there will be a range of particle masses that can be found both in $AR=2$ and $AR=1$, depending on their velocities. We therefore exclude all particles within this mass range.

We start by determining a mass lower limit, such that all particles of higher masses fall only within $AR \geq 2$. This is the mass that creates an ion charge signal equal to the lower charge limit for $AR \geq 2$ of $1.23 \times 10^{-13}$ C, given the slowest calibrated velocity (2 km s$^{-1}$). Fig. 4 of Grün et al. (1995) demonstrates that this mass limit is $\sim 10^{-13}$ kg. We can also calculate this threshold directly using the calibration information provided with the DDS data, and find a lower mass limit of $1.4 \times 10^{-13}$ kg. We thus select only data with mass $> 10^{-13}$ kg. When selecting the particles to include, we do not use the masses provided in the DDS dataset, but instead produce an 'ion charge mass' using the calibration data. The ion charge signal is considered more accurate than the electron charge signal.

Our selection of the data by the class number *CLN* may also affect our radial distribution. $CLN=3$ are always true dust impacts, $CLN=2$ are usually dust impacts, while $CLN=0$ and 1 are usually noise within the inner Jovian region (certainly within ~20 $R_J$). However, outside ~50 $R_J$, all *CLN* classes represent dust impacts. We therefore split the distribution into 0–50 $R_J$ (where we use $CLN=2,3$) and 50–500 $R_J$ (where we use all *CLN* classes: data is too sparse beyond ~500 $R_J$ for our purposes here.

To model the theoretical radial distribution of these sources we require both the number density $n_\infty$ of particles in interplanetary space far from Jupiter and a description for the expected gravitational focusing (given by focusing factor *f*). To convert from *f* to a number of particles, we need also the mean impact velocity $v_{mean}$ and the mean effective sensitive area $A_{eff,mean}$ as functions of distance from Jupiter *r*, as well as the total time $\Delta t(r)$ Galileo spends in each radial bin. The number of particles $N(r)$ as a function of distance from Jupiter *r* is then:

$$N(r) = n_\infty f(r) A_{eff,mean}(r) v_{mean}(r) \Delta t(r) \quad (3)$$

We note that for some very small particles, magnetospheric focusing may be expected, with the effect peaking for particles with radii 0.3–0.4 μm (Colwell and Horányi, 1996). We do not consider such effects here, except to note that the simulations of Colwell and Horányi (1996) produce an increase of up to a factor of ~4 in the number of interplanetary particles that impact Jupiter.

We determine the total time $\Delta t(r)$ that Galileo spends in each radial bin using the Galileo trajectory data. The mean velocity and mean sensitive area as a function of radial distance can be calculated using the noise impacts on the DDS detector. The noise data consist of records that are not considered to be real impacts, and generally are the result of the strong Jovian radiation environment Krüger et al. (1999a). Although they cannot be considered real particles, the noise records do contain information on the Galileo pointing, and position and velocity. The ~33,000 noise data points are distributed throughout the Jovian system, and form a large body of data on the Galileo DDS geometry at each point within the Jovian system. They can thus be used to reconstruct the mean impact velocity and mean sensitive area as a function of radial distance, without having to manually reconstruct the geometry at each point. At the location of each noise impact, we therefore calculate mean impact velocity of detectable interplanetary and interstellar grains at the detector, using the method given in Section 3. We then determine the set of such locations that fall within each radial bin, and subsequently calculate a final mean impact velocity for each radial bin. We apply the same process to the effective sensitive area. There are sufficient data within ~100 $R_J$ for this process to characterise the observability of these populations.

We use the gravitational focusing correction given in Spahn et al. (2006), which is a correction of the formula given by Colombo et al. (1966). However, we adjust the factor $f$ (using $F = Nv_{imp}$, F the flux, N the number density and $v_{imp}$ the impact velocity) such that it describes the increase in the number density rather than in the flux:

$$f(r) = \frac{1}{2}\sqrt{1+\frac{2GM_J}{rv_\infty^2}} + \frac{1}{2}\sqrt{1+\frac{2GM_J}{rv_\infty^2}-\left(\frac{R_J}{r}\right)^2\left(1+\frac{2GM_J}{R_J v_\infty^2}\right)} \quad (4)$$

where $G$ is the gravitational constant, $M_J$ is the mass of Jupiter, $r$ is the radial distance from Jupiter, $v_\infty$ is the dust impact velocity at infinity relative to Jupiter, and $R_J$ is the radius of Jupiter.

The term proportional to $(R_J/r)^2$ is due to shielding by Jupiter and is negligible ($<1\%$ effect) for the dataset considered here: accordingly $f(r)$ reduces considerably to

$$f(r) = \sqrt{1+\frac{2GM_J}{rv_\infty^2}} = \sqrt{1+\frac{v_{esc}^2}{v_\infty^2}} \quad (5)$$

which is the general gravitational focusing equation obtained by Öpik (1951). Here we continue to use the full equation for completeness.

We have two methods available to approximate the number density of interplanetary dust at the distance of Jupiter, but outside the Jovian system. First, we can use the direct method demonstrated in Krivov et al. (2002a), who extrapolate the number of particles detected by the DDS as Galileo approached Jupiter (between 2400 and 500 $R_J$) to predict the expected rate of dust impacts by interplanetary particles closer to the planet. They find 4 impacts in 285 days, for masses $>10^{-14}$ kg and velocities $<10\ \mathrm{km\,s^{-1}}$ (the latter restriction is used because they are attempting to determine the contamination of the fraction of the data with velocities $<10\ \mathrm{km\,s^{-1}}$ by exogenic particles). We find 3 particles with masses $>10^{-13}$ kg in the same region. We use Krüger et al. (1998) to determine that the data completeness factor at this time is about 65%. Combining this with our number of particles gives us a rate of interplanetary particles with masses $>10^{-13}$ kg of ~0.016 per day. We convert this into a number density of $9\times10^{-10}\ \mathrm{m^{-3}}$ using the mean impact velocity near the edge of the Jovian system of $\sim9\ \mathrm{km\,s^{-1}}$.

A second approach is to simply use the ESA Interplanetary Meteoroid Engineering Model 2 (IMEM 2) (Dikarev et al., 2005). We determine the number density of particles with mass $>10^{-13}$ kg on a plate detector at 5.2 AU oriented along the velocity vector with maximum incidence angle 70°. The IMEM model uses five populations to define the dust cloud, including cometary and asteroidal dust each with lifetimes limited by collisions and by Poynting–Robertson drag, and also interstellar dust. At Jupiter the model is dominated by interstellar dust, with cometary dust affected by Poynting–Robertson drag a secondary major component. We find the number density for this cometary population is $2.7\times10^{-10}\ \mathrm{m^{-3}}$, with an average impact velocity of $27\ \mathrm{km\,s^{-1}}$, about three times lower than the direct approach. This appears as a factor of 30 in Fig. 4 given the strong focusing assumed by Krivov et al. (2002a).

This IMEM model can also provide estimates for the interstellar dust, and provides an estimated number density of $1.7\times10^{-11}\ \mathrm{m^{-3}}$. However, the model for interstellar grains is basic. Additionally, the accuracy of IMEM fluxes near Jupiter is severely limited by the lack of dust observations at these distances from the Sun. It is expected that the flux errors in the region 0.4–1.5 AU may be a factor of 3 for all populations (Inter-agency Space Debris Coordination Committee Working Group 2, 2009). Therefore, a more accurate estimate for the interstellar dust (IS) flux is that seen by the Ulysses Dust Detector (identical to the Galileo DDS) and also by Galileo. The flux of IS particles with mass $>10^{-13}$ kg can be estimated from Fig. 11 of Landgraf et al. (2000) to be $1\times10^{-7}\ \mathrm{m^{-2}\,s^{-1}}$ (Landgraf et al., 2000), which can be converted to a number density of $3.6\times10^{-12}\ \mathrm{m^{-3}}$. This is a few hundred times lower than the direct approach of Krivov et al. (2002a).

Fig. 4 demonstrates the number of expected interplanetary and interstellar dust impacts, using both the IMEM and the additional sources of flux information described above. The focusing factor requires a velocity at infinity for each population. For this we use the velocities given by the IMEM subtracted by the velocity of Jupiter of $\sim13\ \mathrm{km\,s^{-1}}$, which produces the maximum focusing possible for these IMEM velocities. The choice of this velocity is not crucial as the focusing effect will be very small, particularly in the outer region of the Jovian system demonstrated in Fig. 4. We can see that the expected theoretical numbers of particles from

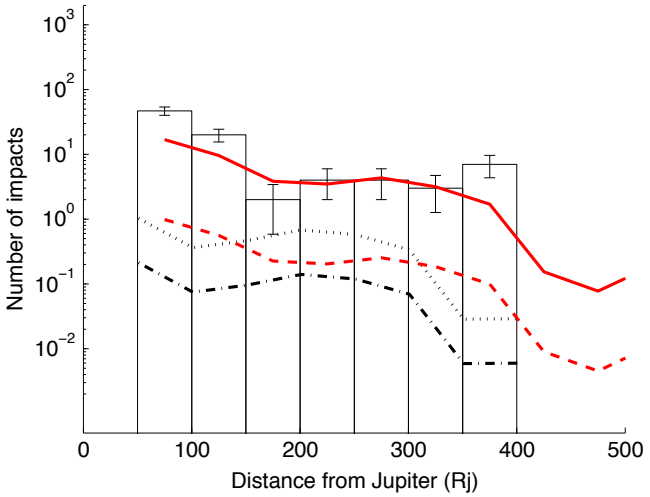


**Fig. 4.** Expected radial distribution of interplanetary and interstellar meteoroids. The red solid and dashed lines are for interplanetary dust, and are based on number density estimates using DDS data far from Jupiter and the method used by Krivov et al. (2002a) (solid line), and the IMEM model (Dikarev et al., 2005) (dashed line). The black dotted and dot-dashed lines depict the interstellar distributions, based on number density estimates far from Jupiter given in the IMEM model (Dikarev et al., 2005) (dotted line), and in Landgraf et al. (2000) (dot-dashed line). All four curves use IMEM velocities to determine the focusing effect. DDS data for particles with estimated masses $>10^{-13}$ kg (the mass that creates an ion charge signal equal to the lower charge limit for $AR \geq 2$) are shown as a histogram. (For interpretation of the references to colour in this figure caption, the reader is referred to the web version of this article.)

both interstellar models and the IMEM model for interplanetary particles are far too small to account for the observed number of DDS impacts. By contrast, it is apparent that the flux of interplanetary impacts as detected by the DDS far from Jupiter is consistent, when focusing is included, with the observed impacts of impacts between 50 and 500 $R_J$ (red solid line in Fig. 4).

Therefore, we only examine the interplanetary dust, as modelled using DDS data at distances 500–2400 $R_J$ and the method of Krivov et al. (2002a), to investigate the possible sources of dust in the inner Jovian region ($<50R_J$). The choice of velocity for the focusing was arbitrarily chosen to be equal to that from the IMEM model. However, we expect a range of velocities is possible. We thus also vary the velocity at infinity between 1 and 6 km $s^{-1}$ (Fig. 5). We have no direct evidence of the existence of such a low velocity population, and as such it is not included in the IMEM model. However, the Trojan asteroids at the 1:1 resonance with Jupiter could be a potential dust source with low velocities at Jupiter.

We find that there is insufficient focusing for the distribution of interplanetary or interstellar grains to reproduce the observed peaked radial distribution in the Galilean satellite region. An interplanetary population with the Krivov number density but with a very low velocity at infinity ($\sim$1 km $s^{-1}$) may be able to explain the peak of the data, but overestimates the expected numbers further from Jupiter. The drop in flux inward of $\sim$8 $R_J$ in Fig. 5 is an artifact associated with the low amount of time Galileo spent in this region. We thus conclude that it is difficult for interplanetary and interstellar dust to be the dominant source of dust in the Galilean satellite region.

### 5.2. Captured interplanetary particles

Colwell et al. (1998b) model the capture of interplanetary and interstellar grains by Jupiter. Colwell and Horányi (1996) demonstrate that the focusing effect from the magnetosphere peaks for particles $\sim$0.3 μm in size. Using numerical simulations of 10,000 particles 0.4–2.0 μm in size, Colwell et al. (1998a) and Colwell et al. (1998b) find that the peak capture rate for interplanetary particles on low-eccentricity, low-inclination orbits occurs for $\sim$0.8 μm grains. The upper limit on the capture rate of 'cometary'-type dust on high-speed orbits is more than an order of magnitude lower than for low-speed grains. Their simulations include the gravity of the Sun and Jupiter, solar radiation pressure and the Lorentz force, and use the magnetospheric model of Horanyi (1994).

Colwell et al. (1998b) found that the captured grains form two populations: a prograde population with inclinations 0–20°, and a retrograde population with inclinations 140°–180°. Due to radiation pressure, the eccentricity undergoes periodic variations that result in a broad eccentricity range between 0 and 1, with most particles having eccentricities below 0.8. There are two clusters of captured particles in semi-major axis also: one at $\sim$3 AU and one between 9–17 $R_J$. Due to the distribution of eccentricities, the radial distribution instead presents clusters at 2–3 $R_J$ and 6–9 $R_J$. This radial distribution allows Colwell et al. (1998b) to calculate an optical depth profile (their Fig. 5).

We test the theoretical model of Colwell et al. (1998b) against the DDS data by converting this optical depth profile (optical depth $\tau$ vs. radial distance) into a plot of number density vs. radial distance. We note Colwell et al. (1998b, 's)'s assumptions of 1 μm grains with 40 year lifetimes, and estimate the vertical extent $L$ of the captured particles from their paper's Fig. 4. The number density $n$ is then:

$$n = \frac{\tau}{\pi s^2 L} \tag{6}$$

where $s$ is the particle radius.

Finally, we use the method detailed in Section 5.1 to estimate the mean impact velocities ($v_{mean}$) and the mean DDS spin-averaged sensitive area ($A_{eff}$) in each radial bin for captured interplanetary particles, as well as the time ($\Delta t$) spent by Galileo in each radius bin. These allow us to determine the number of expected impacts $N$ using a variant of Eq. (3):

$$N(r) = n(r) v_{mean}(r) A_{eff}(r) \Delta t(r). \tag{7}$$

We can directly compare the theoretical $N(r)$ to the number of observed particles (Fig. 6). The expected location of the peak in the theoretical distribution is in approximate agreement with that in the DDS data. However, the theoretical distribution peaks more sharply than the data. We note that there are many sources of uncertainty in arriving at this theoretical distribution. In addition, several concerns arise when interpreting DDS data inside 10 $R_J$: (i) small number statistics, (ii) the noise environment, (iii) changing impact geometry near Galileo's pericentre. Furthermore, the mass bias discussed in Section 5.1 will also apply: namely, that by use of only $AR \geq 2$ we will not count all particles of the included mass range. However, we cannot

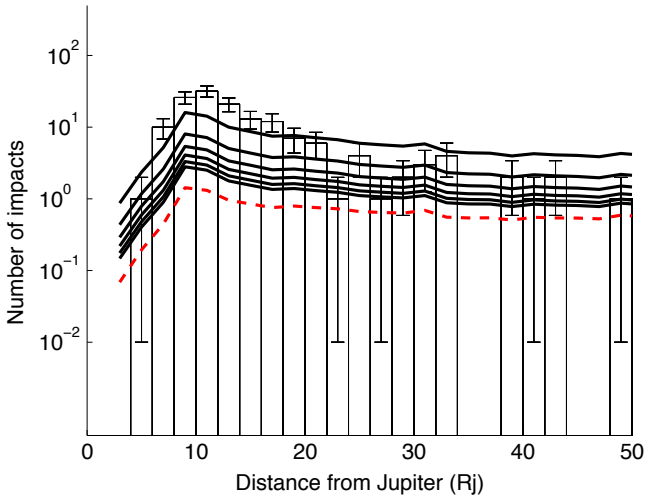


**Fig. 5.** Expected radial distribution of interplanetary meteoroids in the region $\sim$4–50 $R_J$ for different assumptions on their velocity at infinity, from 1–6 km $s^{-1}$ in steps of 1 km $s^{-1}$, using the number density measurements far from Jupiter given by the Krivov et al. (2002a) model. The radial distribution using the Krivov et al. (2002a) number density but the minimum focusing velocity of 13.8 km $s^{-1}$ (based on the IMEM model) is given by the red dashed line. DDS data for particles with masses $>10^{-13}$ kg (the mass that creates an ion charge signal equal to the lower charge limit for $AR \geq 2$) is shown as a histogram. (For interpretation of the references to colour in this figure caption, the reader is referred to the web version of this article.)

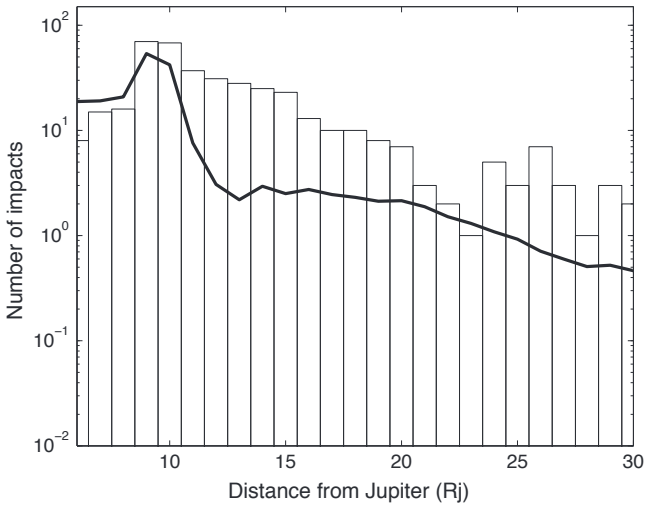


**Fig. 6.** Expected radial distribution of captured interplanetary meteoroids, determined using the theoretical model of Colwell et al. (1998a) (solid line).

correct for this bias because we cannot directly restrict the Colwell model to the mass range $>10^{-13}$ kg. Indeed, Colwell et al. (1998b) demonstrate that most captured particles are in the range 0.6–1.4 μm. Assuming spherical particles of density 2500 kg m$^{-3}$, the upper mass of these grains is therefore $\sim 3\times 10^{-14}$ kg. It is therefore possible for captured grains to fall within $AR=1$, if their impact speeds are less than $\sim 10$ km s$^{-1}$.

Might refinements in the capture modelling alleviate the problem? The steepness of the peak probably follows from the large decelerations that are necessary for the capture process to function efficiently. It is thus likely to be relatively robust in the modelling, and so represent a significant challenge to the hypothesis of captured interplanetary debris. Additionally, with large radii ($\sim 1$ μm) and dominance of retrograde orbits (and thus high impact speeds), we would expect most magnetospherically captured grains to be present in the $AR\geq 3$ charge class; we have confirmed that the $AR\geq 3$ impacts alone also do not match the expected distribution. We conclude that it is unlikely that the observed distribution can be explained primarily by the exact model presented in Colwell et al. (1998b), but that additional modelling is required to fully assess this possible source.

### 5.3. Outer satellite region

Krivov et al. (2002b) find impacts in the outer Jovian system (50–400 $R_J$) that are consistent with expected number densities for impact-generated ejecta from outer satellites. They find that the number density in this region is significantly higher than that at larger distances (Krüger et al., 1998), supporting their argument that these impacts are unlikely to be due to interplanetary particles.

It is difficult, however, to accurately evaluate the radial distribution for these impact-generated ejecta from the outer satellites. This is because there will be additional factors that significantly affect their radial distribution. The orbits of outer satellite grains that reach the Galilean Satellite region will be driven by radiation pressure to high eccentricities. Thus, there will be a strong increase in number density towards the perijove of the eccentric orbits. Additionally, electromagnetic effects would become important near the planet and the processes that govern the survivability of each orbit are difficult to quantify. To create a believable radial distribution we would need to accurately model all sources, sinks, and dynamical forces for dust grains of different sizes; such a model would suffer from large uncertainties in its many input parameters. It is very likely, however, that debris from outer satellites may be more efficiently captured into the inner Jovian system than interplanetary particles, as suggested by energy arguments.

### 5.4. Accelerated escaping dust grains

Tiny $\sim 10$ nm particles from Io have been detected in streams by the Ulysses and Galileo spacecraft, moving at speeds in excess of 200 km s$^{-1}$ (Grün et al., 1993; Zook et al., 1996; Graps et al., 2000). These do not contribute to the radial distribution of $AR\geq 2$ particles because they fall into $AR=1$. Furthermore, due to the steep dependence of $Q_I$ on $v$ (Eq. (1)), larger escaping dust grains have still smaller impact signals. By comparing the velocities of numerically simulated grains accelerated outwards after being launched from Io, we find that the charge is related to the grain mass by $Q\propto m^{-1/6}$, as long as the impact speed is dominated by the particle's speed. Thus submicron-sized grains from Io and the Gossamer rings should not directly contribute to the radial distribution under discussion.

Nevertheless, they may augment the production of impact-generated ejecta clouds at Europa, Ganymede and Callisto. Impacts of tiny 10 nm stream particles onto Europa, Ganymede, and Callisto are perhaps a million times more common and yet still $\sim 1\%$ as energetic as the impact of an interplanetary micron-sized dust grain, making this an appealing energy source. These tiny grains likely sandblast the surfaces of the Galilean satellites quite effectively, but can they loft micron-sized debris? No - this is forbidden energetically by the large escape velocities of the satellites; an 80 nm accelerated particle, for example, has only enough energy to free one 400 nm fragment, and then only if all of its impact energy is partitioned optimally. However, Hamilton and Krüger (2008) and Jontof-Hutter and Hamilton (2012a,b) have shown that under the right circumstances, significant numbers of micron-sized dust grains may be driven to escape from near Jupiter by variable charging effects such as passages through Jupiter's shadow; these large grains can potentially contribute to the radial distribution and the satellite impact flux.

## 6. Directional information: sensitive area

We have already analysed the populations that can be detected at the location of each DDS impact and used the radial distribution

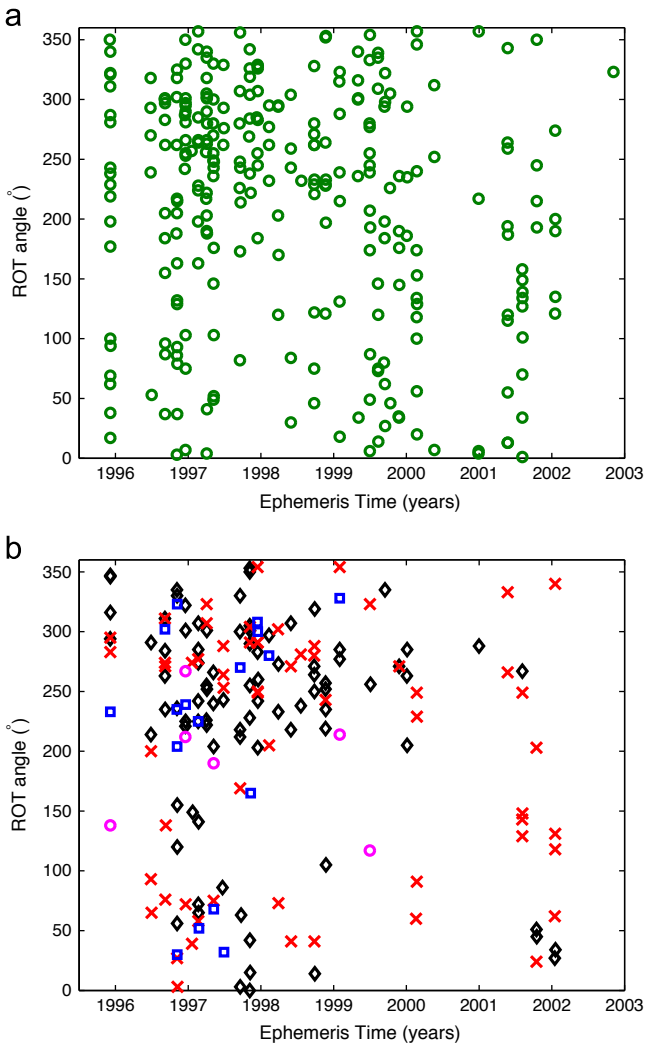


**Fig. 7.** Distribution of data for each *AR* class for time vs. ROT for (a) $AR=2$, and (b) $AR=3$ to 6. ROT (Section 2.1) defines the rotational state of the spacecraft (see main text). Green circles are $AR=2$ data, black diamonds are $AR=3$, red crosses are $AR=4$, blue squares are $AR=5$ and magenta circles are $AR=6$. (For interpretation of the references to colour in this figure caption, the reader is referred to the web version of this article.)

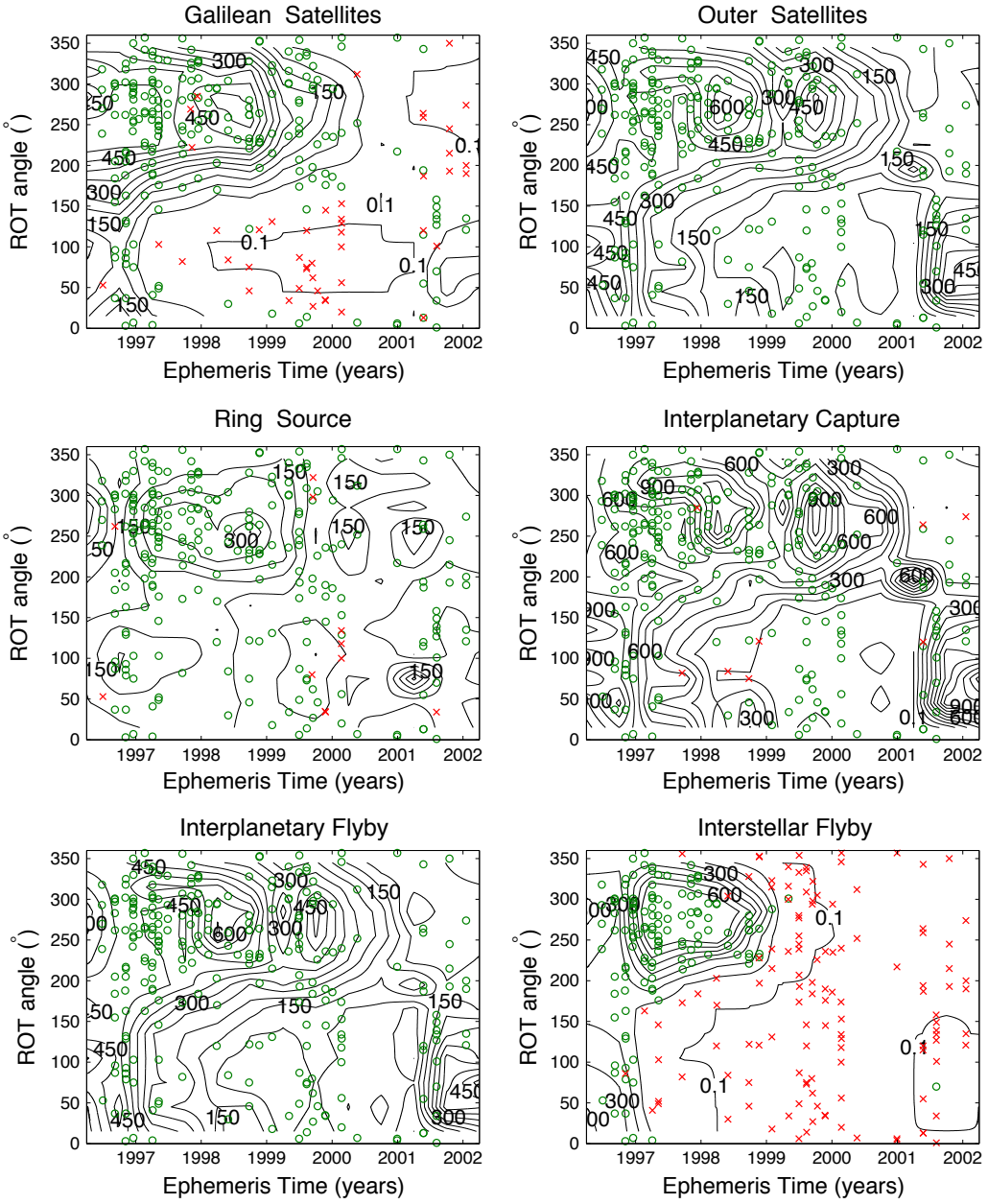


**Fig. 8.** Effective sensitive area for time vs ROT for the six orbital populations of Table 1 (contours). Contours are at values between 0.1 $cm^2$ and the maximum effective sensitive area, and are spaced by levels of 50 $cm^2$ (GS, RS, IF, OS) or 100 $cm^2$ (IC, IS). We then overplot the $AR=2$ impact data that are consistent with each population as solid green circles, and those that are inconsistent as red crosses. (For interpretation of the references to colour in this figure caption, the reader is referred to the web version of this article.)

to demonstrate that is it difficult for two populations (interplanetary and interstellar dust) to fully explain the observations. We now need to determine the most likely remaining population to have been detected at these locations. This requires analysis of the sensitive area of the detector. This allows us to determine the area that each population 'sees' as it approaches the detector: a population that sees a larger area is more likely to be detected. We must be cautious with this approach, however, as this method cannot provide us with information on the existence of the population, only on the likelihood of detecting that population if it does exist. Additionally, our conclusions in this section are only as good as our estimation of the theoretical parameters for each population, given in Table 1, which are also highly uncertain. Uncertainty is also created by the presence of wall impacts, which will expand the regions inside which each population can be observed, blurring slightly the contours in the figures given below (Figs. 8, 9, 11 and 12).

We want to compare the effective sensitive area of the DDS to the distribution of observed impacts with time. For this we use the ROT angle (defined in Section 2.1, and which describes the viewing direction of the detector), as this is our only measure of the impact direction of detected incoming particles. Fig. 7 demonstrates this distribution of particles in ROT angle and time.

### 6.1. Distribution in time and ROT angle

The orbit model described in Section 3 can provide us with the mean sensitive area for the orbits of each population at each Galileo position. As we also have the ephemeris time and ROT angle at each of these positions, we can determine the average of these mean sensitive areas for a given range of ephemeris time and ROT values (Figs. 8 and 9).

There is clearly a difference between the different grain masses, with an excess of $AR=2$ (Figs. 7(b) and 9) particles around

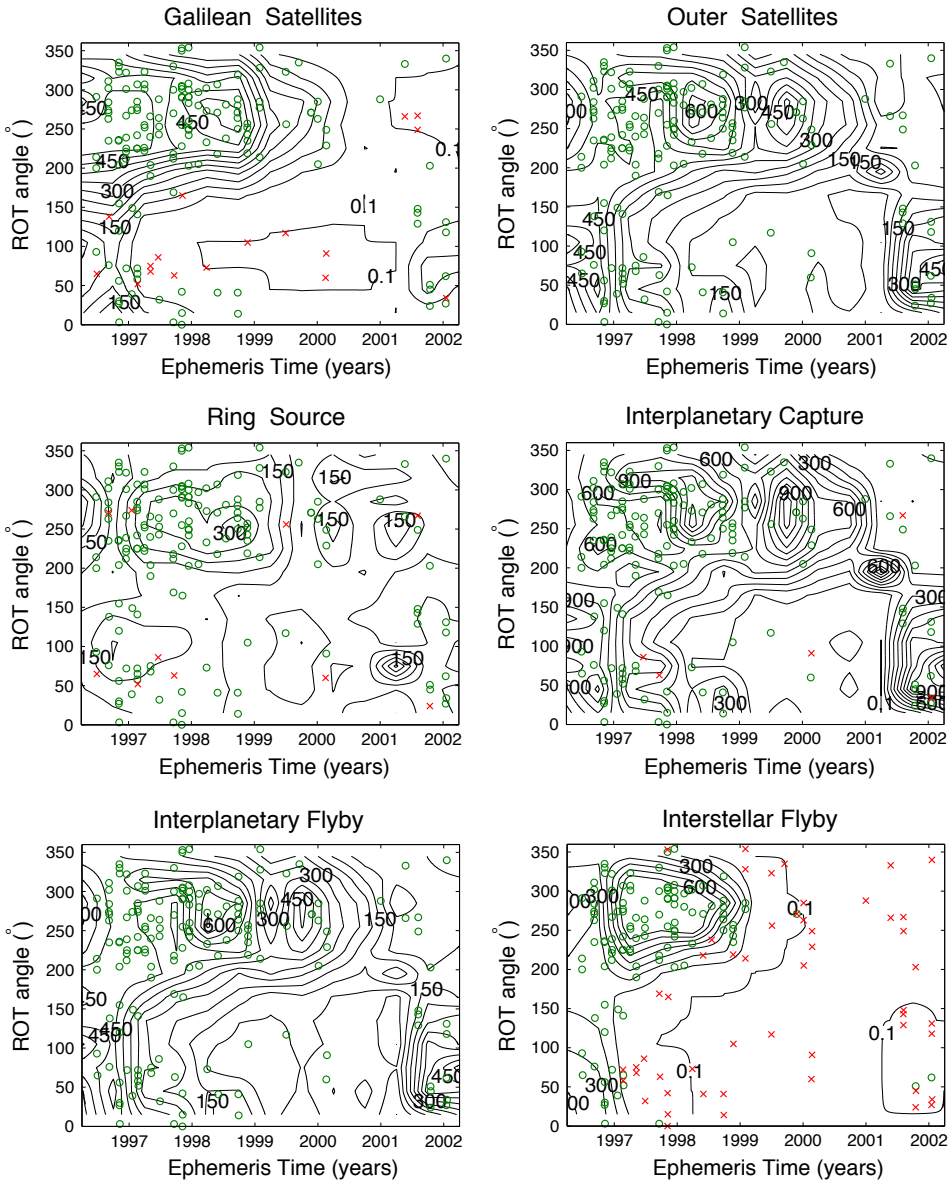


**Fig. 9.** Effective sensitive area for time vs ROT for the six orbital populations of Table 1 (contours). Contours are at values between 0.1 $cm^2$ and the maximum effective sensitive area, and are spaced by levels of 50 $cm^2$ (GS, RS, IF, OS) or 100 $cm^2$ (IC, IS). We then overplot the $AR \geq 3$ impact data that are consistent with each population as solid green circles, and those that are inconsistent as red crosses. (For interpretation of the references to colour in this figure caption, the reader is referred to the web version of this article.)

1999–2000 that is not seen in $AR \geq 3$ (Figs. 7(a) and 8). This indicates that there is a dynamical difference between the impacts described by these different charge classes. There is no one population that appears to best match $AR=2$ data in Fig. 8. $AR \geq 3$ impacts may be best matched to the magnetospherically captured interplanetary particles, which can explain 90% of this source. Alternatively, the distribution is also well fit by outer satellite and interplanetary flyby particles. However, there are insufficient particle numbers to use a chi-square test (or similar) to conclusively determine which population is the best fit to the data. Any attempt at such an approach is further hampered by the similarity in these sensitive area distributions. The similarity is not surprising as dust from both outer satellites and interplanetary flybys have similar speeds and directions near Jupiter. In addition, some of the choices for each population - the radial distance limits for GS and IC, and the restriction to positive radial velocities for RS - mean that on occasion some particles cannot belong to the tested population, even when the sensitive area contours suggest that they should. This results in some red crosses within an area of green circles.

Indeed, there are very few convincing matches between the data and any populations. This implies that there may be more than one dominant population for both $AR=2$ and $AR \geq 3$. With a low number of impacts it is not possible to statistically separate these combinations. Another approach would be to declare, for example, that Galilean satellite ejecta are the dominant source for $AR=2$ impacts, and by removing all impacts that can be described by this source, achieve a set of impacts that must be from a secondary source. Unsurprisingly, one finds that there is still no good population match to the remaining impacts. Possible problems include that some removed impacts are not Galilean satellite ejecta, that the populations are not correctly defined, or that there are additional unconsidered source(s) - but it is not possible to determine which is the case here.

### 6.2. Distribution in the ROT-shift time variable

Previous studies of this data have used the ROT angle and the effective sensitive area to conclude that the data must contain a

fraction of retrograde particles. Grün et al. (1998) concluded that a shift in the ROT angle by ~180° cannot be caused by prograde particles, and must be evidence of retrograde orbits. Colwell et al. (1998a) showed that the distribution of observed impacts during the flyby of Ganymede on Galileo's second orbit matches better to the effective sensitive area for retrograde particles than for prograde particles. Thiessenhusen et al. (2000) concluded that $AR \geq 3$ impacts were a best match to retrograde impacts by showing that the data distribution matched the expected distribution of retrograde particles when plotted against a variable that they called the 'ROT shift time'.

In Fig. 10 we provide the distribution of observed impacts in the parameter 'ROT shift time', which is the time at which the ROT angle for circular planar retrograde impacts would switch from 180°–360° to 0–180°: refer to Thiessenhusen et al. (2000) for further details. This 'ROT shift time' is in effect a combination of the effects of distance from Jupiter, and time throughout the Galileo mission. Although this coordinate choice is designed to search explicitly for retrograde particles, it can provide information on other 'beamed' sources such as the ring source.

Any 'shift' in the ROT angle of $AR=2$ in Fig. 10(a) is difficult to distinguish as there are few impacts with a ROT shift time greater than ~5 days. Low-eccentricity prograde particles should occur mostly at high ROT values (as we see for the Galilean satellite particle distribution in Figs. 8 and 9). Low-eccentricity retrograde particles should be largely confined to the upper left (UL) and lower right (LR) quadrants. This shift from top left to lower right is seen clearly in the $AR \geq 3$ data (Fig. 10(b)).

Could the DDS data set be a result of prograde particles only? In Figs. 11 and 12 we include the sensitive area plots in this ROT shift time frame. As expected, Galilean satellite particles, on low-eccentricity prograde orbits, have mostly ROT angle values greater than 180°. However, a few actual $AR=2$ impacts have lower ROT shift values near the ROT shift time. We can see that most $AR \geq 3$ particles fit this pattern also, with most low ROT angle values occurring very near to the ROT shift time.

Thus, the major difference between the $AR=2$ and $AR \geq 3$ data sets is largely that the $AR=2$ population of impacts has low ROT shift values that occur before the ROT shift time (LL Quadrant), while the $AR \geq 3$ particles do not. These cannot be explained by low eccentricity prograde or retrograde particles: they must be particles on highly eccentric orbits. We have already determined that high eccentricities are required to explain a fraction of $AR=2$ impacts (Section 4). Therefore, it is possible that the major difference is an absence of highly eccentric grains in the $AR \geq 3$ dataset. This does not rule out retrograde magnetospherically captured interplanetary particles as either a dominant or minor source of $AR \geq 3$ impacts, but does demonstrate that there may be an alternative explanation to that provided by Thiessenhusen et al. (2000).

Is it possible that highly eccentric grains are observed in the lower charge $AR=2$ class but not in $AR \geq 3$? To reach $AR \geq 3$, a particle of mass $1 \times 10^{-15}$ kg (about 0.45 μm with density 2500 kg m$^{-3}$) would need an eccentricity greater than 0.5 at 10 $R_J$ and 0.9 at 15 $R_J$. This means than only very massive or very highly eccentric grains can reach $AR \geq 3$. The differences in these distributions hint at contributions from different populations (see Fig. 1, which also highlights the role of $AR=2$ grains on eccentric orbits).

### 6.3. Quadrant analysis in ROT shift time

We conduct a final analysis of the 'ROT shift time' figures, making use of the distribution of impacts shown in Fig. 10. One feature of these plots that is particularly diagnostic of retrograde particles is the relative number of particles found in the lower right (LR) quadrant (those having $ROT < 180°$ and which occur after the ROT shift time). In addition Thiessenhusen et al. (2000) demonstrated that the lower left

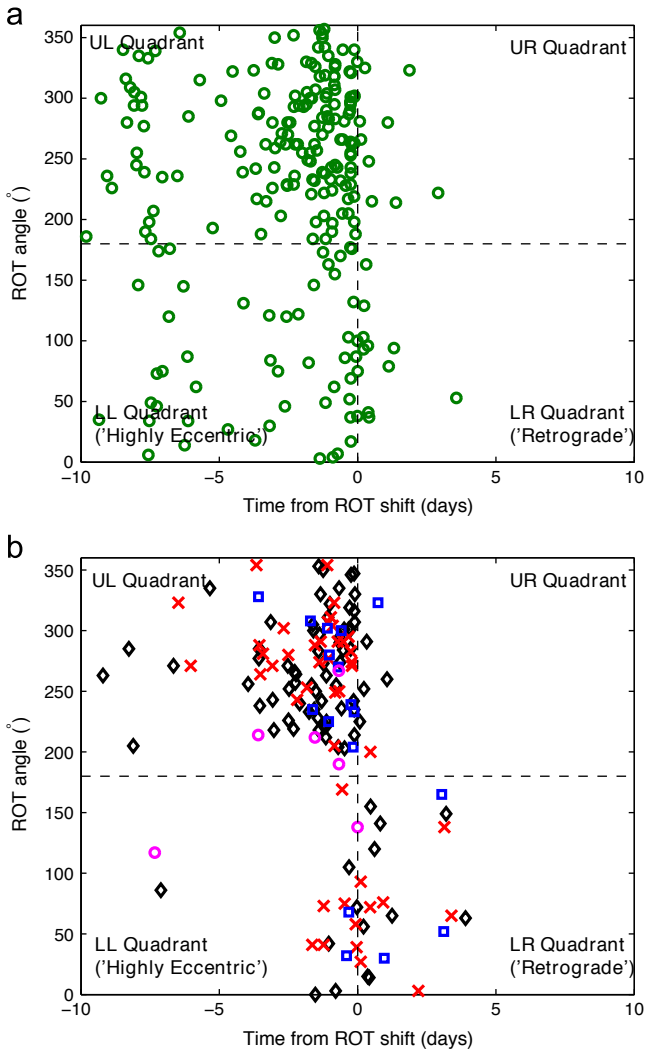


**Fig. 10.** Distribution of data for each *AR* class for ROT shift time vs ROT for (a) AR=2, and (b) AR=3 to 6. ROT (Section 2.1) defines the rotational state of the spacecraft while ROT shift is the time introduced by Thiessenhusen et al. (2000) (see main text). Green circles are $AR=2$ data, black diamonds are $AR=3$, red crosses are $AR=4$, blue squares are $AR=5$ and magenta circles are $AR=6$. Labels demonstrate the four quadrants that can be described by different dynamical populations, as detailed in the text. (For interpretation of the references to colour in this figure caption, the reader is referred to the web version of this article.)

(LL) quadrant (those with $ROT < 180°$ but which occur before the ROT shift time) are highly eccentric particles, not consistent with either prograde or retrograde low eccentricity orbits. We use the relative populations in the LL (indicative of highly eccentric orbits) and LR (indicative of retrograde orbits) quadrants to analyse differences in the AR classes (Table 4).

The LL Quadrant percentage is a particularly diagnostic measure of the importance of highly eccentric grains. This is because highly eccentric particles can occur in all four quadrants, but are by far the dominant population in the lower left quadrant. Therefore, presence of these grains here indicates that highly eccentric grains may be important in all quadrants. We see again that the 'highly eccentric' percentage (LL Quadrant) is significantly higher for $AR=2$ than for any other class in Table 4.

Another striking pattern is that the LR Quadrant, which indicated retrograde particles, is much higher for $AR=4$ than for any other amplitude class in Table 4. This observation is new, as it implies that the retrograde particles are more significant in $AR=4$ than in $AR=3$

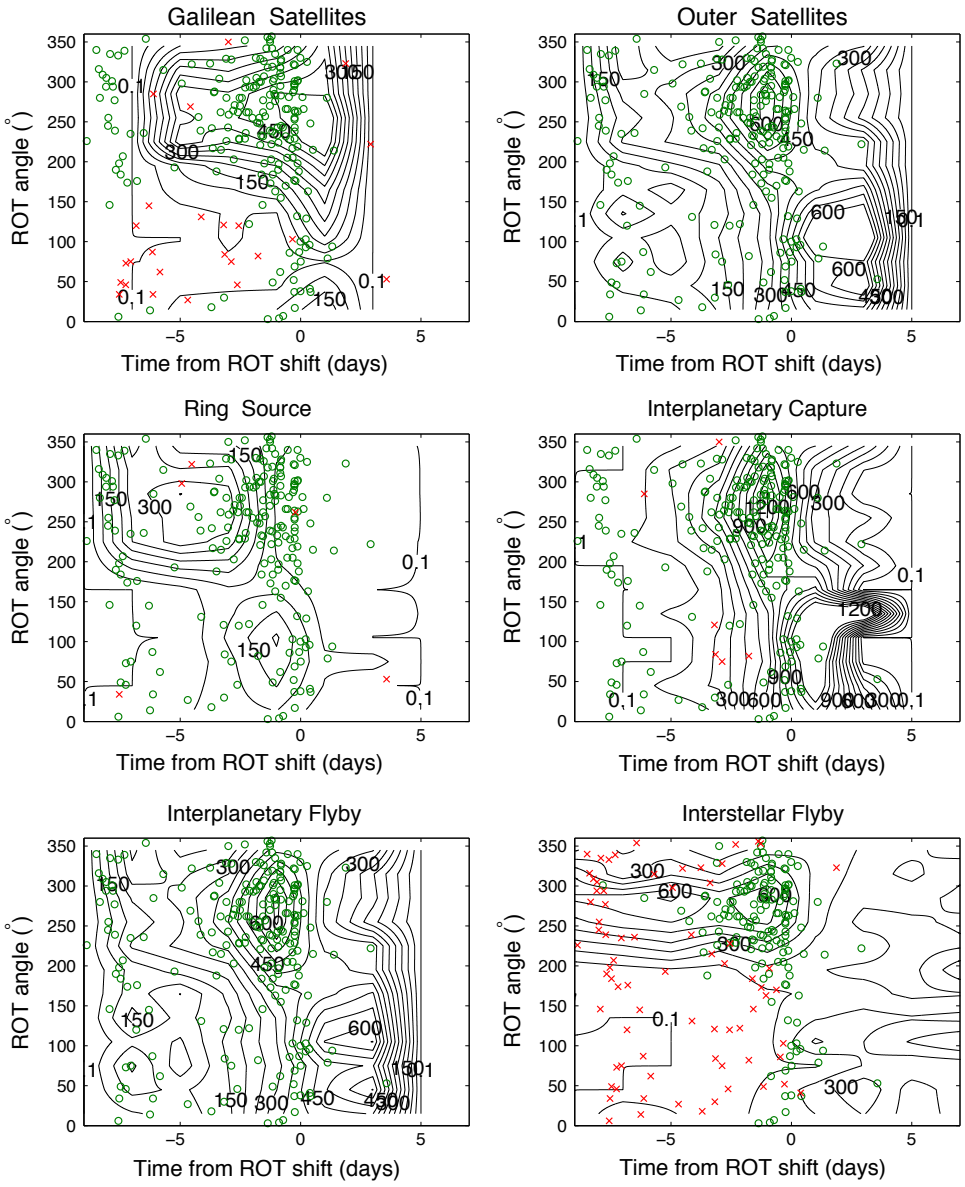


**Fig. 11.** Effective sensitive area for ROT shift time vs ROT for the six orbital populations of Table 1 (contours). Contours are at values between 0.1 $cm^2$ and the maximum effective sensitive area, and are spaced by levels of 50 $cm^2$ (GS, RS, IF, OS) or 100 $cm^2$ (IC, IS). We then overplot the $AR=2$ impact data that are consistent with each population as solid green circles, and those that are inconsistent as red crosses. (For interpretation of the references to colour in this figure caption, the reader is referred to the web version of this article.)

(that is, only for the most massive particles). This does not mean that retrograde particles do not exist in $AR=3$, but only that they preferentially populate the higher AR classes. This result might be expected as retrograde impacts would naturally have very high impact velocities, and thus higher impact charge measurements than prograde orbits. In this case we also expect retrograde particles to be important in $AR=5$, which may be indicated by the elevated 'retrograde' percentage of 18%. However, we note that the small statistics in the $AR=5$ class may affect this result.

There is also a noticeable increase in the percentage of $AR=4$ particles in the 'highly eccentric' LL Quadrant. We can check, also whether $AR=4$ shows signs of having highly eccentric particles by re-examining the data of Fig. 10. We see that the red crosses of the $AR=4$ data do not populate the lower right quadrant well, as most red crosses occur very near to a ROT shift time of zero. By contrast, the $AR=2$ green circles in Fig. 10 span the whole LL Quadrant. Therefore, it is unlikely that $AR=4$ has a significant proportion of highly eccentric grains, as is the case for $AR=2$.

We can compare this result to the results on $AR$ classes in Section 5, which suggested that the observed number of $AR=4$ particles is significantly inflated compared to the number expected if these particles were all from the same source. We can see now that this excess of impacts in $AR=4$ could be because they represent retrograde particles and have correspondingly larger impact speeds, and not Galilean satellite ejecta on prograde orbits.

Our analysis suggests that $AR=4$ contains an excess of particles in LR Quadrant, but not a distribution of particles in the LL Quadrant indicative of highly eccentric particles. We argue that this demonstrates the presence of low eccentricity retrograde particles. Although moderately eccentric prograde orbits are also possible, we consider this a less likely explanation due to the lack of $AR=2$ impacts in the LR Quadrant of Fig. 10. Incomplete data

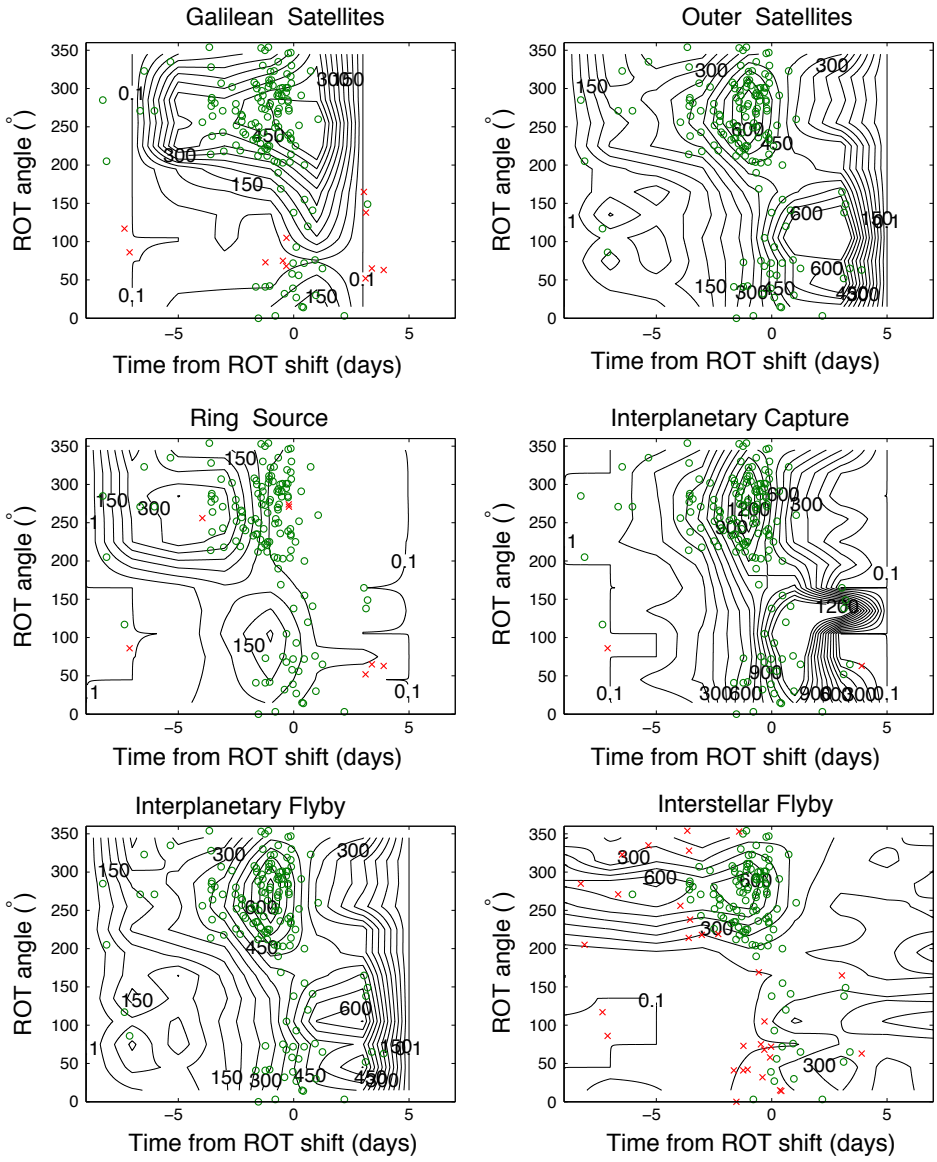


**Fig. 12.** Effective sensitive area for ROT shift time vs ROT for the six orbital populations of Table 1 (contours). Contours are at values between 0.1 $cm^2$ and the maximum effective sensitive area, and are spaced by levels of 50 $cm^2$ (GS, RS, IF, OS) or 100 $cm^2$ (IC, IS). We then overplot the $AR \geq 3$ impact data that are consistent with each population as solid green circles, and those that are inconsistent as red crosses. (For interpretation of the references to colour in this figure caption, the reader is referred to the web version of this article.)

transmission and electronics ageing may affect this conclusion, but we expect that it will not significantly weaken this result.

## 7. Summary and conclusions

In this work we have (i) extended the analysis of DDS data to previously unanalysed data, (ii) considered six potential sources of dust at Jupiter, and (iii) systematically treated orbits with all eccentricities and inclinations. We are not able to determine definitively the nature of the various populations that contribute to the Galileo DDS impacts observed in the Galilean satellite region, other than to confirm that more than one population is required. However, we are able to place limits on the importance of certain populations. We show that eccentricities $>0.1$ are required for at least 10% of $AR=2$ and 5% of $AR \geq 3$ and we demonstrate that a small fraction of $AR=2$ ($\sim$3%) must have eccentricities greater than 0.7.

Using the radial distribution of Fig. 3, we can exclude interplanetary, interstellar and accelerated dust grains from the inner Jovian system as major contributors (though a high flux of very slow ($\sim$1 km $s^{-1}$) interplanetary grains could well explain a fraction of impacts). However, it is difficult to exclude the possibility that these sources contribute to the small number ($\sim$3%) of very highly eccentric $AR=2$ grains required by Fig. 1.

**Table 4**
Fractional population of the quadrants in Fig. 10 as a function of Amplitude Range (AR). In particular, the LL Quadrant is an indicator for highly eccentric grains, and the LR Quadrant is an indicator for retrograde impacts. There are insufficient statistics in the $AR=6$ class to use in this analysis. We include values for the UL and UR Quadrants for completeness.

| Quadrant | AR = 2 | AR = 3 | AR = 4 | AR = 5 |
|---|---|---|---|---|
| Number impacts | 273 | 89 | 60 | 17 |
| UL quadrant (%) | 61 | 73 | 55 | 65 |
| UR Quadrant (%) | 7 | 6 | 7 | 6 |
| LL Quadrant (%) | 24 | 7 | 15 | 12 |
| LR Quadrant (%) | 8 | 14 | 23 | 18 |

These highly eccentric grains could be outer satellite ejecta or captured interplanetary particles.

The sensitive area study also demonstrates that more than one dominant source is required, at least for $AR=2$. The source of high eccentricity $AR=2$ (and $AR\geq 3$) grains is unclear: other impacts may be explained by Galilean satellite ejecta. Our analysis of the sensitive area using the ROT shift time method of Thiessenhusen et al. (2000) demonstrates additional patterns for $AR\geq 3$. In particular, we see evidence for retrograde particles in the $AR=4$ subset of the data, while the $AR=3$ subset does not have such a strong signature (in contrast to the results of Thiessenhusen et al. (2000)). In addition, the number of $AR=3$ particles is about double what we would expect from a mass distribution for a population of ejected particles, if we assume that Galilean satellite ejecta are responsible for $AR=2$ impacts. This suggests that Galilean satellite ejecta can be a dominant contributor to $AR=3$ impacts, but not to $AR=4$ impacts.

Importantly, we have shown that the previously suggested Galilean satellite ejecta and captured interplanetary particles are likely strongly represented in DDS data but are not able to account for all impacts.

## Acknowledgements

We acknowledge support from the Faculty of the European Space Astronomy Centre (ESAC).

## References

Altobelli, N., Kempf, S., Krüger, H., Landgraf, M., Roy, M., Grün, E., 2005. Interstellar dust flux measurements by the Galileo dust instrument between the orbits of Venus and Mars. J. Geophys. Res. (Space Phys.) 110 (July), 7102.

Altobelli, N., Krüger, H., Moissl, R., Landgraf, M., Grün, E., 2004. Influence of wall impacts on the Ulysses dust detector on understanding the interstellar dust flux. Planet. Space Sci. 52 (December), 1287–1295.

Bottke, W.F., Nesvorný, D., Vokrouhlický, D., Morbidelli, A., 2010. The irregular satellites: the most collisionally evolved populations in the solar system. Astron. J. 139 (March), 994–1014.

Burns, J.A., Showalter, M.R., Hamilton, D.P., Nicholson, P.D., de Pater, I., Ockert-Bell, M.E., Thomas, P.C., 1999. The formation of Jupiter's faint rings. Science 284 (May), 1146.

Colombo, G., Lautman, D.A., Shapiro, I.I., 1966. The earth's dust belt: fact or fiction? 2, gravitational focusing and Jacobi capture. J. Geophys. Res. 71 (December), 5705.

Colwell, J.E., Horányi, M., 1996. Magnetospheric effects on micrometeoroid fluxes. J. Geophys. Res. 101, 2169–2176.

Colwell, J.E., Horányi, M., Grün, E., 1998a. Capture of interplanetary and interstellar dust by the jovian magnetosphere. Science 280, 88–91.

Colwell, J.E., Horányi, M., Grün, E., 1998b. Jupiter's exogenic dust ring. J. Geophys. Res. 103, 20023–20030.

Dikarev, V., Grün, E., Baggaley, J., Galligan, D., Landgraf, M., Jehn, R., 2005. The new ESA meteoroid model. Adv. Space Res. 35, 1282–1289.

Göller, J.R., Grün, E., 1989. Calibration of the Galileo/Ulysses dust detectors with different projectile materials and at varying impact angles. Planet. Space Sci. 37 (October), 1197–1206.

Graps, A.L., Grün, E., Svedhem, H., Krüger, H., Horányi, M., Heck, A., Lammers, S., 2000. Io as a source of the Jovian dust streams. Nature 405 (May), 48–50.

Grün, E., Baguhl, M., Hamilton, D.P., Kissel, J., Linkert, D., Linkert, G., Riemann, R., 1995. Reduction of Galileo and Ulysses dust data. Planet. Space Sci. 43 (August), 941–951.

Grün, E., Baguhl, M., Hamilton, D.P., Riemann, R., Zook, H.A., Dermott, S., Fechtig, H., Gustafson, B.A., Hanner, M.S., Horányi, M., Khurana, K.K., Kissel, J., Kivelson, M., Lindblad, B.A., Linkert, D., Linkert, G., Mann, I., McDonnell, J.A.M., Morfill, G.E., Polanskey, C., Schwehm, G., Srama, R., 1996a. Constraints from Galileo observations on the origin of Jovian dust streams. Nature 381 (May), 395–398.

Grün, E., Fechtig, H., Hanner, M.S., Kissel, J., Lindblad, B.-A., Linkert, D., Maas, D., Morfill, G.E., Zook, H.A., 1992. The Galileo dust detector. Space Sci. Rev. 60 (May), 317–340.

Grün, E., Hamilton, D.P., Riemann, R., Dermott, S., Fechtig, H., Gustafson, B.A., Hanner, M.S., Heck, A., Horanyi, M., Kissel, J., Kruger, H., Lindblad, B.A., Linkert, D., Linkert, G., Mann, I., McDonnell, J.A.M., Morfill, G.E., Polanskey, C., Schwehm, G., Srama, R., Zook, H.A., 1996b. Dust measurements during Galileo's approach to Jupiter and Io encounter. Science 274 (October), 399–401.

Grün, E., Krüger, H., Dermott, S., Fechtig, H., Graps, A.L., Zook, H.A., Gustafson, B.A., Hamilton, D.P., Hanner, M.S., Heck, A., Horányi, M., Kissel, J., Lindblad, B.A., Linkert, D., Linkert, G., Mann, I., McDonnell, J.A.M., Morfill, G.E., Polanskey, C., Schwehm, R., Srama, R., 1997. Dust measurements in the Jovian magnetosphere. Geophys. Res. Lett. 24 (September), 2171.

Grün, E., Krüger, H., Graps, A.L., Hamilton, D.P., Heck, A., Linkert, G., Zook, H.A., Dermott, S., Fechtig, H., Gustafson, B.A., Hanner, M.S., Horányi, M., Kissel, J., Lindblad, B.A., Linkert, D., Mann, I., McDonnell, J.A.M., Morfill, G.E., Polanskey, C., Schwehm, G., Srama, R., 1998. Galileo observes electromagnetically coupled dust in the Jovian magnetosphere. J. Geophys. Res. 103 (September), 20011–20022.

Grün, E., Zook, H.A., Baguhl, M., Balogh, A., Bame, S.J., Fechtig, H., Forsyth, R., Hanner, M.S., Horanyi, M., Kissel, J., Lindblad, B.-A., Linkert, D., Linkert, G., Mann, I., McDonnell, J.A.M., Morfill, G.E., Phillips, J.L., Polanskey, C., Schwehm, G., Siddique, N., Staubach, P., Svestka, J., Taylor, A., 1993. Discovery of Jovian dust streams and interstellar grains by the ULYSSES spacecraft. Nature 362 (April), 428–430.

Hamilton, D.P., Burns, J.A., 1993. Ejection of dust from Jupiter's gossamer ring. Nature 364 (August), 695–699.

Hamilton, D.P., Krüger, H., 2008. The sculpting of Jupiter's gossamer rings by its shadow. Nature 453, 72–75.

Hill, J.R., Mendis, D.A., 1979. Charged dust in the outer planetary magnetospheres. I—physical and dynamical processes. Moon Planets 21 (August), 3–16.

Hill, J.R., Mendis, D.A., 1980. Charged dust in the outer planetary magnetospheres. II—trajectories and spatial distribution. Moon Planets 23 (August), 53–71.

Horanyi, M., 1994. New Jovian ring? Geophys. Res. Lett. 21 (June), 1039–1042.

Horányi, M., Morfill, G., Grün, E., 1993. Mechanism for the acceleration and ejection of dust grains from Jupiter's magnetosphere. Nature 363, 144–146.

Humes, D.H., 1980. Results of Pioneer 10 and 11 meteoroid experiments—interplanetary and near-Saturn. J. Geophys. Res. 85 (November), 5841–5852.

Inter-agency Space Debris Coordination Committee Working Group 2, November 2009. Comparison of meteoroid models. Prepared by G. Drolshagen (ESA).

Jontof-Hutter, D., Hamilton, D.P., 2012a. The fate of sub-micron circumplanetary dust grains I: aligned dipolar magnetic fields. Icarus 218 (March), 420–432.

Jontof-Hutter, D., Hamilton, D.P., 2012b. The fate of sub-micron circumplanetary dust grains II: multipolar fields. Icarus 220 (August), 487–502.

Koschny, D., Grün, E., 2001. Impacts into ice-silicate mixtures: ejecta mass and size distributions. Icarus 154 (December), 402–411.

Krivov, A., Jurewicz, A., 1999. The ethereal dust envelopes of the Martian moons. Planet. Space Sci. 47 (January), 45–56.

Krivov, A.V., Krüger, H., Grün, E., Thiessenhusen, K.-U., Hamilton, D.P., 2002a. A tenuous dust ring of Jupiter formed by escaping ejecta from the Galilean satellites. J. Geophys. Res. 107, 5002.

Krivov, A.V., Sremčević, M., Spahn, F., Dikarev, V.V., Kholshevnikov, K.V., 2003. Impact-generated dust clouds around planetary satellites: spherically symmetric case. Planet. Space Sci. 51 (March), 251–269.

Krivov, A.V., Wardinski, I., Spahn, F., Krüger, H., Grün, E., 2002b. Dust on the outskirts of the Jovian system. Icarus 157, 436–455.

Krüger, H., Bindschadler, D., Dermott, S.F., Graps, A.L., Grün, E., Gustafson, B.A., Hamilton, D.P., Hanner, M.S., Horányi, M., Kissel, J., Lindblad, B.A., Linkert, D., Linkert, G., Mann, I., McDonnell, J.A.M., Moissl, R., Morfill, G.E., Polanskey, C., Schwehm, G., Srama, R., Zook, H.A., 2006. Galileo dust data from the jovian system: 1997–1999. Planet. Space Sci. 54 (August), 879–910.

Krüger, H., Bindschadler, D., Dermott, S.F., Graps, A.L., Grün, E., Gustafson, B.A., Hamilton, D.P., Hanner, M.S., Horányi, M., Kissel, J., Linkert, D., Linkert, G., Mann, I., McDonnell, J.A.M., Moissl, R., Morfill, G.E., Polanskey, C., Roy, M., Schwehm, G., Srama, R., 2010. Galileo dust data from the Jovian system: 2000 to 2003. Planet. Space Sci. 58 (June), 965–993.

Krüger, H., Grün, E., Graps, A., Bindschadler, D., Dermott, S., Fechtig, H., Gustafson, B.A., Hamilton, D.P., Hanner, M.S., Horányi, M., Kissel, J., Lindblad, B.A., Linkert, D., Linkert, G., Mann, I., McDonnell, J.A.M., Morfill, G.E., Polanskey, C., Schwehm, G., Srama, R., Zook, H.A., 2001. One year of Galileo dust data from the Jovian system: 1996. Planet. Space Sci. 49 (November), 1285–1301.

Krüger, H., Grün, E., Hamilton, D.P., Baguhl, M., Dermott, S., Fechtig, H., Gustafson, B.A., Hanner, M.S., Horányi, M., Kissel, J., Lindblad, B.A., Linkert, D., Linkert, G., Mann, I., McDonnell, J.A.M., Morfill, G.E., Polanskey, C., Riemann, R., Schwehm, G., Srama, R., Zook, H.A., 1998. Three years of Galileo dust data: II. 1993–1995. Planet. Space Sci. 47 (December), 85–106.

Krüger, H., Grün, E., Heck, A., Lammers, S., 1999a. Analysis of the sensor characteristics of the Galileo dust detector with collimated Jovian dust stream particles. Planet. Space Sci. 47 (August), 1015–1028.

Krüger, H., Hamilton, D.P., Moissl, R., Grün, E., 2009. Galileo in-situ dust measurements in Jupiter's gossamer rings. Icarus 203 (September), 198–213.

Krüger, H., Krivov, A.V., Grün, E., 2000. A dust cloud of Ganymede maintained by hypervelocity impacts of interplanetary micrometeoroids. Planet. Space Sci. 48 (December), 1457–1471.

Krüger, H., Krivov, A.V., Hamilton, D.P., Grün, E., 1999b. Detection of an impact-generated dust cloud around Ganymede. Nature 399 (June), 558–560.

Krüger, H., Krivov, A.V., Sremčević, M., Grün, E., 2003. Impact-generated dust clouds surrounding the Galilean moons. Icarus 164 (July), 170–187.

Krüger, H., Linkert, G., Linkert, D., Moissl, R., Grün, E., 2005. Galileo long-term dust monitoring in the Jovian magnetosphere. Planet. Space Sci. 53, 1109–1120.

Landgraf, M., 2000. Modeling the motion and distribution of interstellar dust inside the heliosphere. J. Geophys. Res. 105 (May), 10303–10316.

Landgraf, M., Baggaley, W.J., Grün, E., Krüger, H., Linkert, G., 2000. Aspects of the mass distribution of interstellar dust grains in the solar system from in situ measurements. J. Geophys. Res. 105, 10343.

Öpik, E.J., 1951. Collision probability with the planets and the distribution of planetary matter. Proc. R. Irish. Acad. Sect. 54, 165–199.

Spahn, F., Albers, N., Hörning, M., Kempf, S., Krivov, A.V., Makuch, M., Schmidt, J., Seiß, M., Sremčević, Miodrag, 2006. E ring dust sources: implications from Cassini's dust measurements. Planet. Space Sci. 54 (August), 1024–1032.

Sremčević, M., Krivov, A.V., Krüger, H., Spahn, F., 2005. Impact-generated dust clouds around planetary satellites: model versus Galileo data. Planet. Space Sci. 53 (May), 625–641.

Sremčević, M., Krivov, A.V., Spahn, F., 2003. Impact-generated dust clouds around planetary satellites: asymmetry effects. Planet. Space Sci. 51 (June), 455–471.

Sterken, V.J., Altobelli, N., Kempf, S., Schwehm, G., Srama, R., Grün, E., 2012. The flow of interstellar dust into the solar system. Astron. Astrophys. 538 (February), A102.

Thiessenhusen, K.-U., Krüger, H., Spahn, F., Grün, E., 2000. Dust grains around Jupiter—the observations of the Galileo dust detector. Icarus 144, 89–98.

Verbiscer, A.J., Skrutskie, M.F., Hamilton, D.P., 2009. Saturn's largest ring. Nature 461 (October), 1098–1100.

Willis, M.J., Burchell, M.J., Ahrens, T.J., Krüger, H., Grün, E., 2005. Decreased values of cosmic dust number density estimates in the Solar System. Icarus 176 (August), 440–452.

Zeehandelaar, D.B., Hamilton, D.P., January 2007. A local source for the Pioneer 10 and 11 circumjovian dust detections. In: Proceedings of 'Dust in Planetary Systems', Kauai, Hawaii, USA. 26–30 September 2005. ESA SP-643.

Zook, H.A., Grün, E., Baguhl, M., Hamilton, D.P., Linkert, G., Liou, J.-C., Forsyth, R., Phillips, J.L., 1996. Solar wind magnetic field bending of jovian dust trajectories. Science 274, 1501–1503.